Aalto University
School of Science
Degree Programme in Engineering Physics

Andreas Holm

UEDGE-predicted impact of molecules on plasma detachment in DIII-D

Master's Thesis
Espoo, April 23, 2018

Supervisor: Professor Mathias Groth
Advisor: Professor Mathias Groth

Aalto University
School of Science
Degree Programme in Engineering Physics

ABSTRACT OF
MASTER'S THESIS

Author: Andreas Holm

Title:
UEDGE-predicted impact of molecules on plasma detachment in DIII-D

Date: April 23, 2018 **Pages:** 70

Major: Engineering physics **Code:** SCI3056

Supervisor: Professor Mathias Groth

Advisor: Professor Mathias Groth

Future fusion power plants will operate in detached divertor conditions to reduce the power loads to the divertor targets to acceptable levels. The onset of divertor detachment is experimentally observed at lower separatrix densities than predicted by simulations, which may potentially be explained by molecular effects. This thesis investigates the impact of including molecules on divertor detachment in DIII-D low-confinement mode plasmas using the edge fluid code UEDGE. Parameter scans in electron separatrix density are carried out for deuterium plasmas with intrinsic carbon impurities. Corresponding scans are carried out with diffusive fluid, deuterium molecules with varying, but spatially constant temperatures included in UEDGE. The model considers molecular dissociation, where the dissociation energy is extracted from the electron energy equation. The Franck-Condon energy is returned through the atom energy equation. The scans were evaluated in configurations with the ion ∇B drift in the direction of the lower divertor excluded and included. The simulations were compared to assess the effect of molecules and drifts on the separatrix density required for outer divertor detachment. Including molecules, but excluding cross-field drifts, resulted in a 25% reduction in separatrix density required for detachment onset. This is an effect of dissociative cooling of the electrons. Increasing the molecular temperature from 0.025 eV to 1 eV was found to shift the onset of plasma detachment to 9% higher separatrix densities. Increasing the molecular temperature increases the total power in the domain, which causes the increase in separatrix density required for detachment. Including drifts increased the separatrix density for detachment by 10%, for the no-molecule simulations. This effect is due to cross-field drifts causing divertor asymmetries toward the inner divertor leg. For the simulations including molecules and considering drifts, a stable, high-density, radiative region formed inside the core domain for $n_{e,sep} > 1.6 \times 10^{19}$ m^{-3}. No increase in separatrix density for divertor detachment was observed. The radiating region inside the core domain is due to drift-driven flows increasing the densities inside the core domain where the strongly radiating impurities become confined. The thesis shows that molecular effects have a pronounced role on divertor detachment in UEDGE. However, further investigations are required to assess the validity of the constants used in the UEDGE molecular model.

Keywords: fusion, plasma, divertor, molecules, plasma detachment

Language: English

Aalto-universitetet
Högskolan för teknikvetenskaper
Examensprogram för teknisk fysik

SAMMANDRAG AV
DIPLOMARBETET

Utfört av: Andreas Holm

Arbetets namn:
Molekylers inverkan på plasmans lösgörande i DIII-D med hjälp av UEDGE

Datum:	April 23, 2018	**Sidantal:**	70
Huvudämne:	Teknisk fysik	**Kod:**	SCI3056
Övervakare:	Professor Mathias Groth		
Handledare:	Professor Mathias Groth		

Framtidens fusionskraftverk kommer verka under förhållanden då plasman är lösgjord från divertorn, och divertorns värmebelastning reducerats markant. Experimentellt observerade separatrix-densiteter för plasmans lösgörande är lägre än vad som förutses av fluid-simulationer, och kan delvis vara ett resultat av molekylära processer. Detta arbete utvärderar molekylers inverkan på plasmans lösgörande i svagt sammanhållna DIII-D plasman med hjälp av multifluidkoden UEDGE. Plasmans egenskaper undersöks som funktion av elektronernas separatrix-densitet för deuterium-plasman med kolorenheter. Simulationer utförs i UEDGE med diffunderande, fluida deuterium-molekyler med olika, i rymden konstanta, temperaturer exkluderade samt inkluderade. Den molekylära modellen i UEDGE beaktar dissociation av molekyler till två atomer, som minskar elektronfluidens energi med dissociationsenergin. Atomfluidens energi ökar med Franck-Condon energin i dissociationsprocessen. Simulationerna utförs med jonernas ∇B-strömningar i riktning mot den nedre divertorn exkluderade samt inkluderade. Simulationernas resultat jämförs och molekylernas samt strömningarnas effekt på plasmans lösgörande från den yttre divertorn utvärderas. Separatrix-densiteten för lösgörande minskar med 25% då molekyler inkluderas, för de strömningsfria simulationerna. Detta är ett resultat av elektronernas dissociativa energiförlust. Då molekylernas temperatur ökas från 0.025 eV till 1 eV ökar separatrix-densiteten för plasmans lösgörande med 9%. En ökning i molekylernas temperatur resulterar i en ökning av plasmans totala energi, som leder till högre separatrix-densiteter för plasmans lösgörande. Då strömningar beaktas ökar separatrix-densiteten för lösgörande med 10%, för simulationer exkluderande molekyler. Detta beror på en asymmetrisk förskjutning av plasmans densitet mot den inre divertorn orsakad av strömningarna. För simulationer som inkluderar molekyler och strömningar uppstår en stabil, starkt radiativ region med hög densitet i kärnan då $n_{e,sep} > 1.6 \times 10^{19}$ m^{-3}. Ingen förändring i separatrix-densiteten för plasmans lösgörande observeras. Den radiativa regionen är ett resultat av strömningar, som ökar densiteten i plasmans kärna var radiativa orenheter fängslas. Atbetets slutsats är att molekylära processer har en uppenbar inverkan på plasmans lösgörande i UEDGE. Dock bör vidare arbeten undersöka huruvida de konstanter som används i UEDGE är välgrundade.

Nyckelord:	fusion, plasma, divertor, molekyler, plasmans lösgörande
Språk:	Engelska

Acknowledgements

The day I have always known is coming, but never really expected, is here, as I am finishing this thesis. There are so many people who deserve credit for me making it to this point. My family, who has supported me during the tough times and shared my joy at every success. Joanna, who has been the supportive voice of reason during all my undertakings at Aalto. Teknologföreningen, which has provided me with uncountable opportunities, challenges, successes, and lifelong friendships. This section is too short to mention everyone of you by name, but I still want to say: thank you.

This work would not have been possible without the help of General Atomics and Lawrence Livermore National Laboratory. Not only am I thankful for the professional help of the staff, but also for all the interesting conversations over lunches.

I would like to especially thank Thomas Rognlien for all the time he has invested in helping me with UEDGE, and plasma modeling in general, over the last years. Tom's hospitality has been overwhelming, and I extend my heartfelt thank you to you, Tom.

Lastly I would like to thank Professor Mathias Groth who, with his passion for the field, professionalism, and expertise, has been an irreplaceable mentor over the last years. Mathias' support has allowed me to develop and grow as a physicist and person, and provided me with amazing opportunities to further my career as a researcher. Thank you for the support, as a mentor and a friend, Mathias.

After experiencing the passion, expertise, and kindness of the researchers in the field of fusion technology, I am certain any and all challenges will be overcome. It is merely a question of when - rather than if - fusion power will be our primary source of energy.

Otaniemi, April 23, 2018

Andreas Holm

Contents

Chapter 1

Introduction

The global energy demand is expected to rise by 30% between today and year 2040 due to increased energy demand in India and developing Southeast-Asian economies [1]. The energy required to meet the increased demand cannot be produced from fossil sources as man-made climate change has an increasingly pronounced effect globally, with potentially devastating consequences if carbon-dioxide emission increases from present levels [2]. One prospective substitute for power production is fusion power. Fusion power is based on forging new nuclear bonds and is the process that power stars. Fusion power has several advantages compared to fission power: hydrogen as the fusion fuel is abundant and readily available in most parts of the world [3], the delicate equilibrium in fusion reactors are not susceptible to runaway events, the fusion waste is not radioactive, and fusion has energy densities eclipsing those of conventional power plants. The main drawback of fusion power is its technological complexity: the principle of fusion is based on light nuclei tunneling through the Coulomb barrier formed between charged nuclei in order to create a heavier nucleus. Sufficient tunneling probabilities are required for power productions, which are achieved at high densities and temperatures exceeding 110 million Kelvins, or 10 keV.[1] The high temperatures required for fusion reactions fully ionizes the fuel, which becomes a fully ionized gas known as a plasma, the fourth state of matter.

There are several principles for achieving the required densities and temperatures, and competing machine designs for each principle. This work considers magnetic confinement fusion, where the fusion plasma is suspended in magnetic fields, as in the tokamak device DIII-D. In its diverted configuration secondary magnetic coils are used to create a magnetic null, the X-point, and open magnetic field lines terminating at the vessel walls (Fig. 1.1). The

[1]The convention within the field is to use electron volts as the unit of temperature will be used henceforth in this work

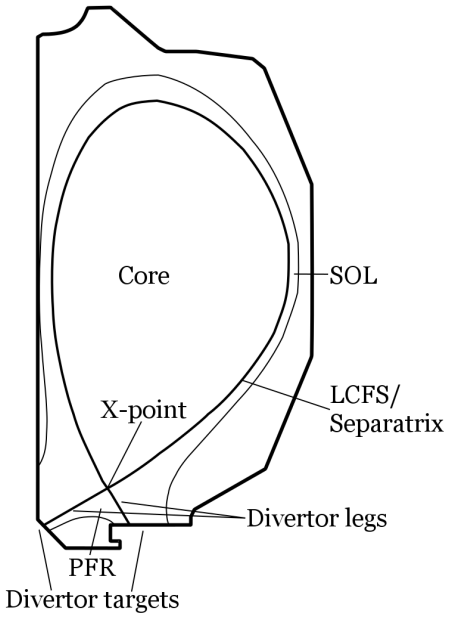

Figure 1.1: A schematic of the poloidal cross-section of a fusion plasma in DIII-D. The regions of the diverted tokamak configuration are marked.

surface where the magnetic field lines terminate, the divertor targets, are designed to withstand plasma surface interaction (PSI). The magnetic configuration separates the divertor chamber and PSI from the plasma core. Various methods, such as impurity seeding, can be utilized in the divertor chamber to reduce the power flux to the plasma-facing components (PFC) to within the material limits, allowing the PFCs to sustain prolonged plasma operation of the fusion device.

The prospective operational mode of future fusion reactors is the *detached regime*, where a cushion of neutral atoms and molecules is formed in front of the divertor targets. The detachment of the plasma occurs once the plasma temperatures at the targets reach < 1 eV through volumetric radiation losses. The heat flux density incident on the PFCs is greatly reduced at such a low plasma temperature as neutral gas impede the flow of plasma, at temperatures around 100 eV, onto the target plates. The forming of a neutral cushion is believed to be strongly dependent on volumetric recombination in the divertor region, occuring at low temperature and high density. Studies have found that dissociative and molecule assisted recombination rates can be significantly higher than electron ion recombination. Thus, understanding the impact molecules has on the divertor conditions may be crucial in understanding and controlling detachment in present and

future fusion devices.

Future fusion devices are assessed and designed based on predictive computer simulations since plasma conditions vary with the device size. Presently, reactor conditions cannot be reached in existing devices. Accurately predicting the operating conditions and the heat fluxes to the PFCs is key to successful and prolonged operation of next generation devices. There are several numerical codes written for predicting the plasma properties in the *scrape-off layer* of fusion plasmas. These plasma *edge codes* have the capability of modeling fusion-relevant plasmas in different geometries including intrinsic and seeding impurities. The most established edge codes are SOLPS [4], EDGE2D-EIRENE [5, 6], and UEDGE [7]. The former two codes model the plasma species as fluids and molecules and atoms are considered by the kinetic EIRENE code package [8].

However, kinetic modeling of molecules and atoms is a computationally significant task. Additionally, the coupling of the kinetic and fluid codes means that numerical convergence cannot be achieved. For sufficiently collisional plasmas, fluid modeling of molecules and atoms can qualitatively predict the plasma properties [9, 10, 11]. The advantages of using a multi-fluid code over coupled kinetic codes are the capability of modeling non-linear processes in significantly shorter run times and steady-state convergence to double-digit computer precision. The multi-fluid code UEDGE [7] has been used to investigate the effect considering molecules has on the steady-state plasma solution.

This thesis is built around the following sections: chapter 2 outlines fusion power production, the tokamak, and the scrape-off layer. A detailed description of the physics model and equations solved by UEDGE is presented in chapter 3 and the UEDGE simulations are described in chapter 4. The results of a comparative study of UEDGE simulations without cross-field drifts excluding and considering molecules in the fusion plasma are presented in chapter 5. The results of representative analysis of the effects of drifts for the same setups are also presented in chapter 5. Chapter 6 discusses the findings of the work, the main conclusions of which are presented in chapter 7.

Chapter 2

Background

2.1 Fusion principles

Fission and fusion power are based on the principle of mass change releasing energy according to Einstein's famous theorem $\Delta E = \Delta mc^2$. The mass difference of the products compared to the reactants is released as kinetic energy distributed between the products. The fusion reaction is facilitated by the strong interaction, which has a range in the order of 10^{-15} m, or femtometers. Thus, for a fusion reaction to take place, the reactants need to be brought within this range of each other for the nuclei to fuse. However, the charged nuclei exert strong Coulomb repulsion on each other. The net potential of the Coulomb and strong interaction results in a *Coulomb barrier* and a potential well within the range of the strong interaction [12]. The size of the Coulomb barrier depends on the product of the nuclear charge of the reactants [12]. Thus, lighter elements have a lesser potential to overcome, although the barrier of two hydrogen nuclei is still of the order of hundreds of keV. Due to *quantum mechanical tunneling* through the Coulomb barrier, there is a finite probability of fusion reactions occurring at energies below the potential of the Coulomb barrier. The probability of a fusion reaction to occur by quantum mechanical tunneling can be described by the fusion cross-section ($[\sigma] = m^2$) [12].

The reaction rate per unit volume, $R = n_i n_j \langle \sigma v \rangle$, is dependent on the reactant number densities (n_i and n_j) and the expectation value of the reactivity

$$\langle \sigma v \rangle \sim \int_v f(v)\sigma(v)v\mathrm{d}v \sim \int_0^\infty e^{-\frac{E}{k_B T}-2G}, \tag{2.1}$$

assuming a Maxwell-Boltzmann velocity distribution of the reactants:

$$f(v) \sim v^2 e^{-\frac{mv^2}{2k_b T}}, \tag{2.2}$$

where m is the particle mass, k_B the Boltzmann constant, T the ambient temperature, v the relative velocity of the fusing nuclei, and G the tunneling probability.

Fusion is the process that powers the stars. The stellar fusion chain is, however, not replicable on earth due to its small fusion cross-section. In stars the small cross-section is mediated by high number densities, facilitated by their immense gravity and hence referred to as gravitational confinement fusion. Controlled, man-made fusion relies on hydrogenic fusion as the prospective source of energy due to the high energy yield and comparatively high reaction rates of the reactions at low temperatures compared to other fusion reactions [12, 13, 14]. Future fusion power plants are expected to operate using *deuterium* and *tritium* (D-T) as fuel. Deuterium and tritium are hydrogen isotopes of mass 2 au and 3 au, respectively. However, tritium is an unstable isotope, undergoing a β-decay with a half-life of 12.32 years, making naturally occurring tritium a scarce resource. Thankfully, tritium can be readily bred from Lithium, using neutrons (tritium breeding) [14]. The D-T reaction yields energetic neutrons, which can be used for tritium breeding in breeding blankets that surround the reactor vessel of future fusion devices.

The low-energy β-emission also pose licensing concerns since tritium can react with oxygen to form tritiated water which, when ingested, poses a radiation hazard. Since tritium is retained in the PFCs of fusion devices D-T operation causes regulatory restrictions, health concerns, and necessitates maintenance periods in reactor operation. As a result, presently most fusion reactors operate with D-D fusion, permitting ease of operation. Benefits of deuterium operation are the abundant availability of deuterium in water and the scalability of the D-D reaction power yields to that of D-T fusion by a factor of 210, validating D-D projections of D-T performance [15].

2.2 Thermonuclear fusion

Thermonuclear fusion is based on providing the energy required to achieve fusion power production by sufficient tunneling through the Coulomb-barrier as thermal energy. The fuel is heated to temperatures of 10 keV and reaches a plasma state: the fuel becomes a fully ionized gas consisting of positive ions, and electrons. Fusion plasmas are assumed to be quasineutral:

$$n_e = \sum_j Z_j n_j, \tag{2.3}$$

where n are the densities, the subscripts e and j refers to electrons and the ionic species, respectively, and Z to the charge state of the corresponding

ion. Due to the presence of free charges in the plasma, interior electric fields are screened within a distance of the order of the *Debye length* ($\lambda_{Debye} = \sqrt{\epsilon_0 kT_e/n_e e^2}$, where T_e is the electron temperature and e the elementary charge) [13]. In tokamaks the Debye length is typically of the order of 10^{-4} m. Outside the Debye length, plasmas are neutral and display *collective behavior* due to the electromagnetic (EM) interaction between the plasma species [14]

The ultimate goal of fusion research is to produce net power, which occurs when the thermal output of a fusion reactor exceeds the input heating power. The ratio of thermal fusion power to the applied input power is defined as the gain factor $Q = P_{in}/P_{fusion}$. For net power production, or *break-even*, to occur Q must exceed unity. Future fusion power plants must, therefore, operate at $Q > 100$. So far, the highest gain factor achieved is $Q = 0.62$ in JET [15], whereas ITER is projected to achieve $Q = 10$.

The ideal operational space for fusion power plants is at *ignition*, when no external power is needed and the fusion power carried by the confined fusion α particles is sufficient to overcome the power losses to create a self-sustained burning plasma: $Q \to \infty$. The *triple product* is an extension of the *Lawson criterion* [16] and describes the conditions required to achieve ignition. The triple product describes a dependency on temperature. The minima for D-T fusion occurs around $T = 15$ keV, for which the triple product can be expressed as [14]

$$nT\tau_E > 5 \times 10^{21} \text{ m}^3\text{s}^{-3}\text{keV}, \tag{2.4}$$

where τ_E is the plasma energy confinement time.

Magnetic confinement fusion (MCF), which is based on the principle of using electromagnetic fields to confine the plasma for prolonged times ($\tau_E \approx$ several seconds) at low pressure ($n \approx 10^{20}$ m^{-3}, $T \approx 15$ keV), has emerged as the front-runner for fusion power production and is the focus for this work.

2.3 The tokamak

The tokamak is a well-established design, which has been developed and researched since the 1960s due to its relatively simple design and axisymmetry. It confines the plasma in a toroidal EM field generated by planar toroidal field coils (Fig. 2.1). According to the Lorentz force, assuming $\mathbf{E} = \mathbf{0}$, the charged plasma is confined in the directions perpendicular to the magnetic field, and is free to move in the parallel direction. In a tokamak the plasma is confined in the parallel direction by closing the field lines on themselves in a toroidal magentic field ($\mathbf{B}_\Phi$).

According to *Ampere's law* the magnetic field is stronger at the toroidal axis where the coils are denser. Thus the inboard and outboard sides of

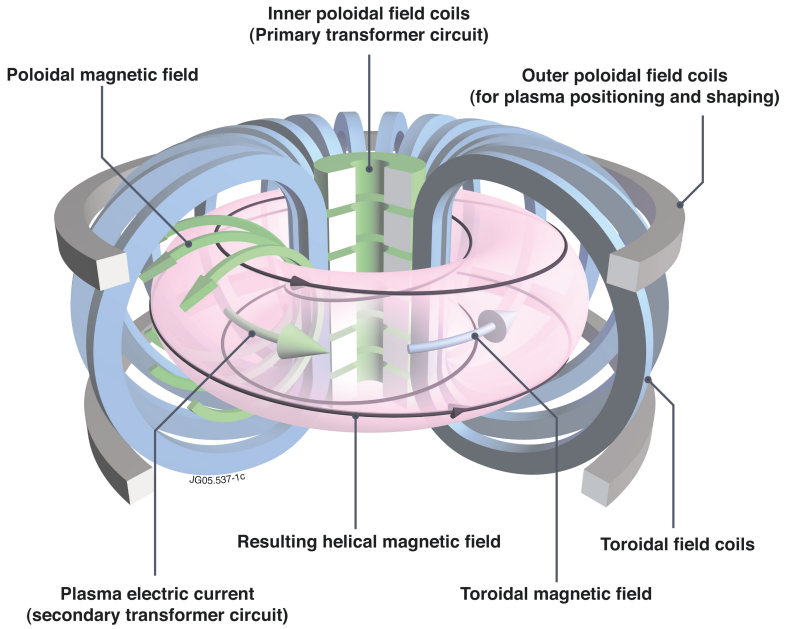

Figure 2.1: A schematic of the magnetic coils and resulting fields in a tokamak. The main engineering and field components are marked. Courtesy of EUROfusion [17].

the poloidal cross-section are commonly referred to as the *high* and *low-field sides* (LFS and HFS), respectively. This non-uniformity induces a $\mathbf{B} \times \nabla B$-drift [13], which results in *charge separation* in the plasma due to the oppositely charged electrons and ions. The resulting electric field induces an $\mathbf{E} \times \mathbf{B}$-drift [13] radially outwards from the toroidal axis, which leads to loss of plasma confinement. In order to alleviate charge separation a poloidal magnetic field ($\mathbf{B}_\theta$) is generated. This is accomplished by a central solenoid at the toroidal axis of symmetry inducing a toroidal current (I_Φ) in the plasma, which acts as the secondary circuit, and in turn generates the poloidal magnetic field component. The plasma confinement in tokamaks is, however, also affected by other drifts. For example, due to the curvature of the magnetic field *curvature drifts* [13] are also present in tokamaks.

The resulting helical field has magnetic field lines, which close on themselves, creating nested *flux surfaces*. The flux surfaces approach a single magnetic field line, the *magnetic axis* [14], at the center of the torus where the pressure is at its maximum. For steady-state operation of tokamaks, the two forces acting on the plasma, the magnetic force and the plasma pressure must balance [13], resulting in flux surfaces of constant pressure. Due to engineering restrictions on the current, the poloidal magnetic field is typically

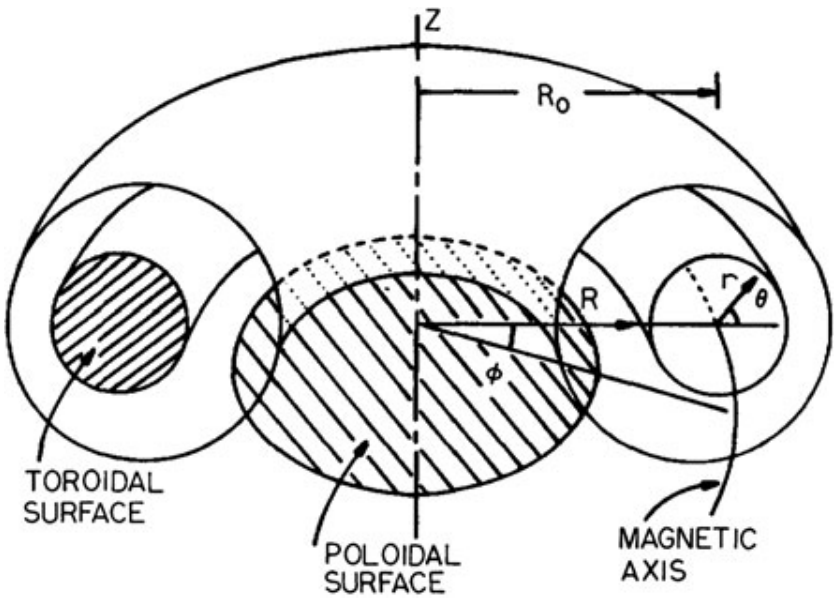

Figure 2.2: Schematic of the tokamak coordinate system [3].

small compared to the toroidal magnetic field ($B_\theta \approx 0.1 B_\Phi$), resulting in a small *magnetic pitch angle* (B_θ / B_Φ).

The axisymmetry of the toroidal tokamak allows for spatial locations to be defined by tokamak coordinates (Fig. 2.2). The coordinates Φ and θ describe the *toroidal* and *poloidal angle*, respectively. The distance between the axis of symmetry and the magnetic axis is referred to as the *major radius* (R) and the distance from the magnetic axis is referred to as the *minor radius* (r). The *parallel direction* refers to the direction parallel to the magnetic field lines and the *parallel distance* commonly used to define distance in the parallel direction. The half-distance between the targets along the parallel field lines, the *connection length* $L \approx \pi R q$, is a common figure of merit for tokamak devices.

Poloidally diverted tokamaks have a magnetic topology with an X-point separating the main chamber from the divertor chamber (Fig. 1.1). The poloidal magnetic equilibrium is now defined by a *last closed flux-surface* (LCFS), commonly referred to as the *separatrix* (Fig. 1.1). The LCFS separates the closed flux surfaces of the confined *core* region from the open flux surfaces which are referred to as the *scrape-off layer* (SOL), discussed below. The open flux surfaces are diverted away from the core plasma into the *divertor* and terminate at the *divertor targets* (Fig. 1.1). The separatrix intersect with the inner and outer targets (IT and OT, respectively) and are referred to as the *inner* and *outer* (or high-field side and low-field side) *strike points*

(ISP and OSP), respectively. The radial positions of the separatrix at the height of the magnetic axis in the poloidal plane are defined as the *inner* and *outer midplane* (IMP and OMP), respectively.

Particle and power transport in the direction normal to the flux surfaces is referred to as *cross-field transport*. The cross-field transport in tokamaks has been found to exceed classical and neoclassical predictions and is dominated by *turbulent transport*. Tokamaks have been found to operate at different modes depending on the core heating power, with better confinement at higher input power and density (*high-confinement mode*) [18]. However, high-confinement mode plasmas exhibit transient events (*edge-localized modes* [19]). This work investigates *low-confinement mode* plasmas in the DIII-D tokamak, and does not treat high-confinement mode processes.

2.4 The scrape-off layer

The scrape-off layer, or SOL, is the narrow region surrounding the plasma core and links the core plasma to the PFCs. The plasma species flow in the parallel direction along the open field lines in the SOL at their respective thermal velocities ($v_{\parallel,j} = c_{s,j} = \sqrt{2k_B T_j/m_j}$, where the subscript j refers to the plasma species) [13]. Typical thermal velocities in the SOL for deuterium ions and electrons are $v_{\parallel,i} \approx 10^4 - 10^5$ m s^{-1} and $v_{\parallel,e} \approx 10^6$ m s^{-1}, respectively. The turbulence-driven cross-field transport creates a steady flux of particles and energy across the separatrix into the SOL, of the order $v_\perp = 1$ m s^{-1} [18]. The low $v_\perp/v_\parallel$ ratio results in PSI taking place predominantly on a narrow, relative to the connection length, area close to the strike points: $A_{PSI} \approx 2(2\pi R)\lambda_{SOL}$. Additionally, the parallel velocity can be split into components in toroidal and poloidal direction (v_Φ and v_θ, respectively) where the ratio v_Φ/v_θ is determined by the ratio B_Φ/B_θ. Since $B_\theta \approx 10B_\Phi$ in present tokamaks, the velocity in the toroidal direction is much greater than the velocity in the poloidal direction. Thus, the analysis of tokamaks are usually carried out on the poloidal cross section of the device where the poloidal projections of velocities are considered, under the assumption of toroidal uniformity due to $v_\Phi \gg v_\theta$.

A property unique to the divertor SOL is the existence of a *private flux region* (PFR), defined as the plasma volume contained below the separatrix in the divertor legs (Fig. 1.1). The PFR is magnetically isolated from the core plasma by the X-point, and the only plasma and heat source into the PFR are cross-field transport across the separatrix from the common SOL. Due to the absence of a PFR-core interface and the relatively small area available for cross-field transport from the SOL, the PFR plasmas have significantly

lower temperatures and densities compared to the main SOL. As a result the ionization rates in the PFR are low and atom and molecule densities are expected to be high in the PFR.

Following conservation of energy, all power transported over the separatrix from the core is deposited onto the vessel walls. Principally, the power in tokamaks is deposited onto the PFCs as kinetic and potential energy over the small area A_{PSI}. The power flux incident on the plates must be maintained within the material limitations of the PFCs, typically considered to be 10 MW m^{-2}, to maintain the integrity of the divertor targets. The focus of tokamak edge physics is hence on SOL predictions and its control. One principal aim of edge physics is to predict and alleviate the effects of sputtering, melting and fuel embedding at the targets. Common methods for decreasing the incident target heat flux density is to alter the magnetic topology in an effort to spread the heat flux over a wider divertor area and seeding radiating impurities in the divertor leg with the aim of radiating power without quenching the core plasma.

The scrape-off layer has been observed to operate at different power exhaust regimes, with different dominating mechanisms. These regimes are dependent on the *SOL collisionality parameter* (ν_{SOL}) which roughly describes the average number of elastic self-scattering events of the plasma particles before being deposited onto the divertor plates [18]

$$\nu_{SOL} = \frac{L}{\lambda_{mfp}} \approx 10^{-16} \frac{L n_e}{T^2}, \tag{2.5}$$

where λ_{mfp} is the mean free path of the ions and electrons and $[T] = \text{eV}$.

The electron thermal velocity and conductivity are higher than that of the ions due to their lower mass (assuming $T_e \approx T_i$), resulting in faster particle and heat transport to the targets compared to the ions. Thus, the initial influx of electrons on the divertor plates causes the plates to become negatively charged. This gives rise to a region of an ambipolar electric field, referred to as the *sheath*. The sheath acts as a high power filter for the electrons, as only the electrons with sufficient energy to overcome the electric repulsion reaches the plate. Thus, the sheath cools the electron population along the SOL, and increases the ion energy in the sheath. However, the total energy reaching the targets is equivalent to the power reaching the *sheath edge* (SE) [18].

Fluid codes commonly model the plasma up to the sheath edge, where the ambipolar plasma flow reaches at least sonic velocity ($v_{SE} \geq c_s = \sqrt{(T_e + T_i)/m_i}$) according to the *Bohm criterion* [20]. The total parallel heat flux density ($q_\parallel$) incident on the SE is limited by the electron and ion *sheath heat transmission coefficients* (γ_e and γ_i, respectively). The sheath

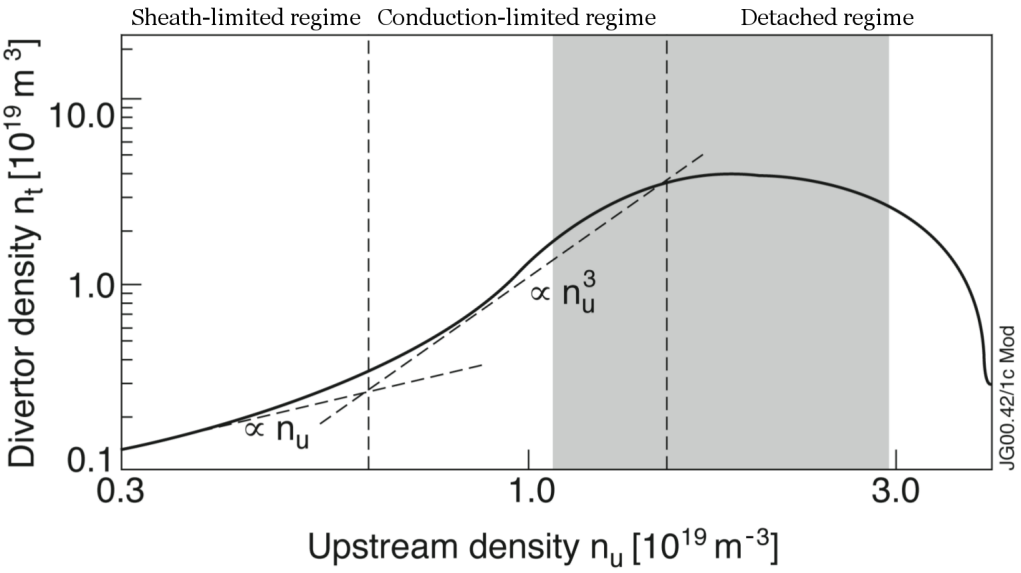

Figure 2.3: Figure outlining the target density dependence on upstream density. Note the logarithmic axes [17].

heat transmission coefficients are convenient approximations for the power removed from the electron and ion channel through potentials caused by the sheath and the Bohm condition ($\gamma_e \sim 4.5 - 5.5$ and $\gamma_i \sim 1.5 - 3$ [18, 21]).

2.4.1 The scrape-off layer regimes.

The behavior of the SOL can be described by three distinct regimes, depending on the collisionality parameter of the SOL [18].

2.4.2 Low ν_{SOL}: the sheath-limited regime

At low SOL collisionality power is transported in the parallel direction by thermal convection. Power enters at the *upstream location*, referring to a location above the divertor legs where power can be considered to enter the SOL, and is deposited at the divertor targets, the *downstream location*. The advective nature of convective heat transport results in a flowing, isothermal ($T_{up} = T_{down}$) plasma with small parallel ion and electron temperature gradients. The sheath-limited regime can be identified by the plasma target density being approximately proportional to the upstream density (Fig. 2.3). Sheath-limited plasmas are often sparse and hot, with significantly different electron and ion temperatures at the targets due to the low frequency of

ion-electron interaction. Due to the high target temperatures inducing high heat fluxes and significant target sputtering and erosion, the sheath-limited regime is not considered reactor-relevant.

2.4.3 Intermediate $\nu_{\mathbf{SOL}}$: the conduction-limited regime

At intermediate SOL collisionality heat transport is dominated by conduction, which can be described by the *Spitzer-Härm heat conductivity* [22].

The conducted heat flux density is dominated by the electrons due to their smaller inertia, and the heat is transported along the parallel direction by parallel heat flux gradients, cooling the plasma species along the parallel distance of the SOL.

As a result of conductive heat transport dominating, the downstream temperatures decrease below the required temperature to ionize the atoms recycled at the target. Thus, ionization occurs within the SOL resulting in a volumetric plasma source in front of the sheath. The cycle of recombination at the target and volumetric ionization forms a thin (compared to L) volume of high recycling. Thus, the regime is also referred to as the *high recycling regime*. The outflow of recycled atoms and molecules from the plate results in a build-up of density at the targets which is approximately proportional to the cube of the upstream density (Fig. 2.3), and decreased target temperatures. Although the peak divertor temperatures in the conduction-limited regime are decreased to ~ 5 eV, the strongly increasing target density and incident particle flux to the target plate are sufficient to increase the incident heat flux above the PFC limitations. Thus, the conduction-limited regime is not considered as a viable operational regime for fusion power production.

2.4.4 High $\nu_{\mathbf{SOL}}$: the detached regime

At high SOL collisionality the target temperatures decrease sufficiently ($T_t <$ 1 eV), through increasing density and volumetric power losses, for *volumetric recombination* of ions and electrons, to occur. This additional plasma sink off the targets results in the buildup of an atom and molecule density in front of the targets with predominantly neutral atoms and molecules incident on the targets, a characteristic of the detached regime. Due to the neutral cushion in front of the targets the target plasma density decreases as a function of upstream density (Fig. 2.3). The incident ions reaching the cushion are cooled by ion-atom friction, thereby transferring their momentum to the atoms by *charge exchange* (CX) reactions. These processes result in pressure and power losses, which reduce the heat flux density incident on the target to within the PFC limits as power is mainly transported by cool, drifting atoms and

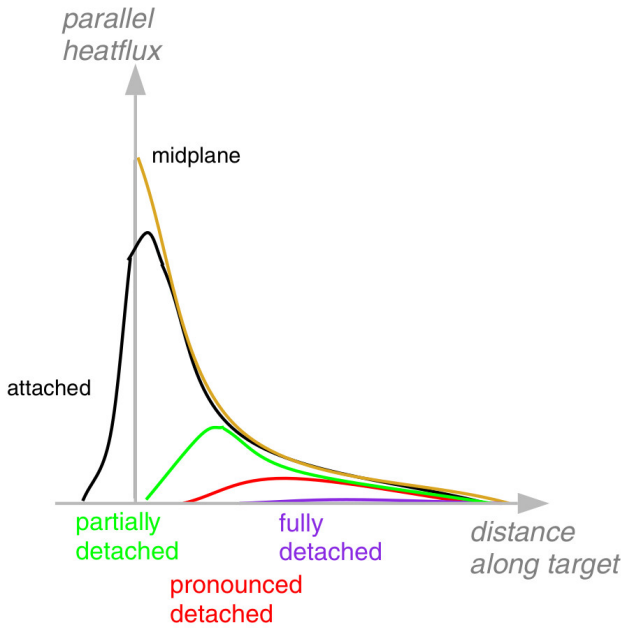

Figure 2.4: Schematic of plasma detachment regimes [23].

molecules. Thus, the detached regime is a prospective operational regime for ITER, and future fusion power plants.

2.5 Plasma detachment

To ensure sufficient lifetime of the divertor in future fusion power plants, operation under *partial* detachment is required. Partial detachment is defined as a significant reduction in heat flux and pressure in the parallel (to the magnetic field lines) direction between the OMP and target for the first few (≈ 2) power decay lengths in the SOL (Fig. 2.4). Here, the power decay length is defined as the decay factor of the exponential fit to the radial profile of the parallel heat flux density at the OMP. Partial detachment typically starts at the strike points and evolves radially outwards. For very low peak power loads and detachment over several power widths detachment is considered to be *pronounced*, with the far SOL plasma still attached (Fig. 2.4). To achieve a reduction in plate particle current over the entire divertor a volume of neutral atoms and molecules up to the vessel walls is required, which is described as *full* divertor detachment (Fig. 2.4). Since the inner target detaches at lower upstream separatrix densities than the outer target, due to the longer connection length over the top of the device, in standard

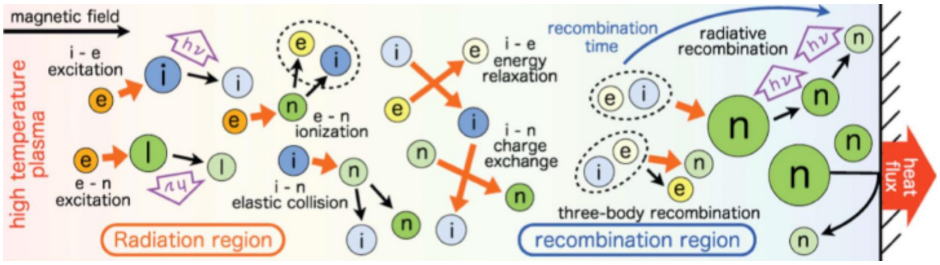

Figure 2.5: Schematic outlining the processes taking place in fusion plasmas. The plasma power is assumed to enter at the upstream location (left side) and is dissipated along the connection length (horizontal direction) and deposited at the target (right side). Here, darker particle color indicates more energy carried by the particle [25].

conditions, the outer target is considered the most critical location. [23]

The decrease in ion flux to the targets is due to neutral atoms and molecules, unaffected by the magnetic fields, forming a shielding volume in front of the divertor targets. In order for a neutral cushion to form, the target temperatures need to be considerably below the ionizing potential of the atoms (13.6 eV for hydrogen). In practice, detachment occurs at target temperatures below ≈1 eV and at high densities. At these conditions volumetric recombination of the plasma becomes significant, and is considered to play a central role in divertor detachment [24].

To achieve sufficiently low temperatures for detachment to occur, power dissipation must occur between the upstream and target locations. Principally, power in fusion plasmas is dissipated by radiative power losses, as particles tend to be deposited onto the targets and walls in a localized fashion. The main power dissipation processes in fusion plasmas are presented in figure 2.5. *Line radiation* of hydrogen and impurity ions are significant radiative processes processes in fusion plasmas. Line radiation occurs when bound, excited electrons of hydrogen and impurity atoms or partially ionized impurities relaxes by photon emission (Fig. 2.5). In the case of hydrogen line radiation the dominant radiative process is *Lyman-alpha* (Ly-α) radiation [26]. Impurities of higher atomic number are strongly radiating over a wider temperature range than hydrogen due to higher ionization potentials and, thus, more electronic levels at higher temperatures. The line radiation power increases with density and excitation processes in the plasma. Thus, in order to achieve detachment *seeding impurities* can be injected into the divertor legs to radiate power in the SOL and achieve detachment at lower upstream temperatures.

There are several volumetric recombination processes taking place in

fusion-relevant plasmas and, thus, playing a role in divertor detachment. The principal processes are *radiative recombination* and *three-body recombination*, together referred to as *electron-ion recombination* (EIR) (Fig. 2.5). In radiative recombination an electron and ion combine to form an atom where the ionization potential, also referred to as the binding energy, released excites the atom. The formed atom then undergoes a radiative relaxation cascade, resulting in the binding energy being radiated away. In three-body recombination an ion reacts with two electrons to form an atom and an electron with a continuous kinetic energy distribution [24].

There are also additional recombination processes, such as *charge-exchange recombination*, *dissociative recombination* of molecular ions, and *molecule assisted recombination* (MAR) [24]. MAR and dissociative recombination are processes related to molecular hydrogen and, more specifically, to rovibrational and molecular ions, respectively. It has been found that the MAR rate can significantly exceed the EIR rates [27], indicating that molecules may play a role in the onset of divertor detachment.

Molecules also play a role in fusion-relevant plasmas through other processes, in addition to recombination. The *dissociation* of molecules and molecular ions into atoms, ions, or a combination of both is an immediate result of molecules in fusion plasmas. Molecules can be dissociated by electrons or ions when the energies are sufficient to break the intramolecular bonds. When a molecule is dissociated the resulting products are born with an associated energy, the *dissociation energy*. The dissociation energy is supplied by the reactants, and a fraction of this energy is carried by the resulting products, based on the *Franck-Condon principle*. The Franck-Condon principle states that electronic transitions are instantaneous compared to the molecular time scale. Thus, when a molecule is dissociated the products must be compatible with the rovibrational momenta of the molecule and position. The energy required for the products to be compatible with the molecular rovibrational state and position is the *Franck-Condon energy* and is carried by the products. Thus, molecular dissociation transfers energy from the reactants, and the products retain the Franck-Condon energy, and acts as a molecule sink and atom or ion source, depending on the process [28].

The ionization of atoms or partially ionized impurities is facilitated by energetic electrons (Fig. 2.5). The ionization potential needs to be supplied by the electron to free a bound electron. Thus, ionization is an electron power sink, and binding energy is transferred to the formed ion as potential energy. This energy is released upon recombination as the kinetic energy of the products of three-body recombination or lost as radiation in radiative recombination processes. If the ion reaches the wall or target the binding energy is deposited onto the target as the ion undergoes surface recombination.

Chapter 3

Methods

3.1 Modeling scrape-off layer plasmas

Plasma transport occurs in a six-dimensional spatial-velocity phase-space, and is therefore said to be a *kinetic phenomenon*. Plasma physics can be considered as a closure of Maxwell's equations by means of *constitutive relations*: expressions for the charge density ρ_c and the current density $\mathbf{j}$ in terms of the electric and magnetic fields $\mathbf{E}$ and $\mathbf{B}$. Let $\mathcal{F}_j(\mathbf{x}.\mathbf{v}, t)$ be the exact phase-space density of plasma species j at point $(\mathbf{x}, \mathbf{v})$ at time t normalized such that:

$$\int \mathcal{F}_j(\mathbf{x}, \mathbf{v}, t)\mathrm{d}^3\mathbf{v} = n_j(\mathbf{x}, t). \tag{3.1}$$

Thus the constitutive relations can be expressed as

$$\rho_c = \sum_j e_j \int \mathcal{F}_j(\mathbf{x}, \mathbf{v}, t)\mathrm{d}^3\mathbf{v}, \tag{3.2}$$

$$\mathbf{j} = \sum_j e_s \int \mathbf{v}\mathcal{F}_j(\mathbf{x}, \mathbf{v}, t)\mathrm{d}^3\mathbf{v}. \tag{3.3}$$

Phase-space conservation requires that

$$\mathbf{D}_j\mathcal{F}_j = \left(\frac{\partial}{\partial t} + \mathbf{v}\nabla + \frac{Z_\sigma e}{m_\sigma}(\mathbf{E} + \mathbf{v} \times \mathbf{B}) \cdot \nabla_v\right)\mathcal{F}_j = 0 \tag{3.4}$$

where $\mathbf{D}_j$ represents the phase-space derivative for species j, ∇ the real-space operator, ∇_v the velocity-space gradient operator, $j \in \{e, i, n, Z\}$, and e, i, n and Z are the electrons, ions, neutral and impurity species, respectively. [29]

Solving equations 3.1–3.4 requires determining $\mathcal{F}_j$ in terms of the electromagnetic fields, for which theoretical formulations exists. However, equation 3.4 considers all scales without statistical averaging of the particle ensemble, thus, $\mathcal{F}_j$ describes the motion of discrete particles and considers the field resulting from these particles. Solving equations 3.1–3.4 constitutes formulating a classical EM many-body problem too large to be solved. Instead a kinetic equation in spatial and velocity space can be derived using *ensemble-averaging* [29].

Let $f_j \equiv \langle \mathcal{F}_j \rangle_{ensemble}$, resulting in equation 3.4 becoming the ensemble-averaged kinetic equation

$$\mathbf{D}_j f_j = \left(\frac{\partial}{\partial t} + \mathbf{v}\nabla + \frac{Z_\sigma e}{m_\sigma}(\mathbf{E} + \mathbf{v} \times \mathbf{B}) \cdot \nabla_v \right) f_j = \mathbf{C}_j(f), \tag{3.5}$$

where $\mathbf{C}_j(f)$ is the *collision operator* of species j, which describes particle encounters of j with like-particles and other species. The collision operator is not necessarily linear and usually involves the distribution function of all interacting species, signified by omission of the argument subscript [29].

3.1.1 Fluid modeling and the Braginskii equations

Solving equation 3.5 exactly is, however, still a computationally significant task. Additionally, the attained species distribution functions contain vastly more information than relevant, or necessary, for plasmas considered for fusion applications. The sheath-limited to conduction-limited regime transitions occurs at $\nu_{sol} \approx 10$ and conduction-limited to detached regime transition occurs at $\nu_{SOL} \approx 100$ [18], at which point fluid analysis of the plasma can be applied. At such conditions the *plasma fluid equations*, derived by taking velocity ($\mathbf{v}$) moments of equation 3.5, can be used to solve equations 3.2 and 3.3. This reduces the problem to three dimensions, which is computationally preferable. Additionally, the fluid approximation results in quantities relatable to experimental observations, such as densities, temperatures and flow velocities [29] .

The zeroth order moment is the *(number) density* (n_j), the first moment the *particle flux density* ($n_j \mathbf{V}_j$), the second order moment the *stress tensor* ($\mathbf{P}_j$), and the third moment the *energy flux density* ($\mathbf{Q}_j$). The conventionality is to express the second and third moments in the species' rest frame ($\mathbf{w}_j \equiv \mathbf{v} - \mathbf{V}_j$, where $\mathbf{V}_j$ is the *flow velocity*), thus, describing the *pressure tensor* ($\mathbf{p}_j$) and the *heat flux density* ($\mathbf{q}_j$), respectively. Similar treatment of the collision operator when considering plasma *particle*, *momentum*, and *energy conservation* yields the *friction force* ($\mathbf{F}_{jj'}$) and the *kinetic energy change*

($W_{jj'}$) between particle species j and j'. Here, $W_{jj'}$ considers the energy transfer between species through collisions and viscous friction [29].

These velocity moments of equation 3.5 produce a set of *incomplete* fluid equations: each higher order moment introduces another unknown. For *collisional*, *unmagnetized* plasmas, which are considered in this work, the *Chapman-Enskog closure scheme* [30] can be applied to the particle mean free paths. The resulting three first velocity moments in a parallel-radial (cross-field) **B** coordinate system are the *Braginskii equations* for electrons and ions [31]:

$$\frac{\partial n_e}{\partial t} + \nabla \cdot (n_e \mathbf{V}_e) = 0, \tag{3.6}$$

$$m_e n_e \frac{\mathrm{d}\mathbf{V}_e}{\mathrm{d}t} + \nabla p_e + \nabla \cdot \boldsymbol{\pi}_e + e n_e (\mathbf{E} + \mathbf{V}_e \times \mathbf{B}) = \mathbf{F}, \tag{3.7}$$

$$\frac{3}{2}\frac{\mathrm{d}p_e}{\mathrm{d}t} + \frac{5}{2} p_e \nabla \cdot \mathbf{V}_e + \boldsymbol{\pi}_e : \nabla \mathbf{V}_e + \nabla \mathbf{q}_e = W_e, \tag{3.8}$$

$$\frac{\partial n_i}{\partial t} + \nabla \cdot (n_i \mathbf{V}_i) = 0, \tag{3.9}$$

$$m_i n_i \frac{\mathrm{d}\mathbf{V}_i}{\mathrm{d}t} + \nabla p_i + \nabla \cdot \boldsymbol{\pi}_i - Z e n_i (\mathbf{E} + \mathbf{V}_i \times \mathbf{B}) = -\mathbf{F}, \tag{3.10}$$

$$\frac{3}{2}\frac{\mathrm{d}p_i}{\mathrm{d}t} + \frac{5}{2} p_i \nabla \cdot \mathbf{V}_i + \boldsymbol{\pi}_i : \nabla \mathbf{V}_i + \nabla \mathbf{q}_i = W_i, \tag{3.11}$$

where $p_j = n_j T_j$, $\mathrm{d}/\mathrm{d}t$ is the *material derivative* and Z is the ion species charge. Here, $\boldsymbol{\pi}_j$ is the *generalized viscosity tensor* $\boldsymbol{\pi}_j = \mathbf{P}_j - p_j \mathbf{I}$, where $\mathbf{I}$ is the unit tensor, and

$$\boldsymbol{\pi}_j : \nabla \mathbf{V}_j \equiv (\pi_j)_{\alpha\beta} \frac{\partial (V_s)_\beta}{\partial (x)_\alpha}. \tag{3.12}$$

In equation 3.12 α and β refer to tensor indices.

The Braginskii equations are for a single ion species of charge Z and ignores any source and sink terms from interactions with neutral gas, which are added in section 3.2.

The closure scheme constitutes

$$(\pi_j)_{\alpha\beta} = -\eta_j \left(\frac{\partial (V_j)\alpha}{\partial (x)_\beta} + \frac{\partial (V_j)_\beta}{\partial (x)_\alpha} - \frac{2}{3} \nabla \cdot \mathbf{V}_j \delta_{\alpha\beta}. \right) \tag{3.13}$$

and

$$\mathbf{q}_{\parallel e} = -K_{\parallel e} \nabla_\parallel T_e - 0.71 \frac{T_e \mathbf{j}_\parallel}{e}, \tag{3.14}$$

$$\mathbf{q}_{\parallel i} = -K_{\parallel i} \nabla_\parallel T_i, \tag{3.15}$$

where η_j and K_j are the *viscosity* and *thermal conduction coefficients*. Here, only the parallel heat fluxes are considered as they dominate over the perpendicular heat fluxes for strong magnetic fields ($\omega_c \tau_{coll} \gg 1$). Turbulent heat fluxes dominated the perpendicular transport in edge modelling as presented in section 3.2.

Following the same derivation the collision operator moments become

$$\mathbf{F}_{\parallel} = \frac{ne\mathbf{j}_{\parallel}}{\sigma_{\parallel}} - 0.71n\nabla_{\parallel}T_e, \tag{3.16}$$

$$W_i = \frac{3m_e}{m_i}\nu_{eq}n(T_e - T_i), \tag{3.17}$$

$$W_e = -W_i + \frac{j^2}{\sigma_{\parallel}} - 0.71\frac{\mathbf{j}\cdot\nabla T}{e}, \tag{3.18}$$

where $\mathbf{j} = -ne(\mathbf{V}_e - \mathbf{V}_i)$ is the net plasma current, ν_{eq} the rate of Coulomb energy exchange collisions, and $\sigma_{\parallel}$ the *parallel electric conductivity*. Here, the particle species are assumed to be at thermal equilibrium and as a result their distribution functions are *drifting Maxwellian distributions*.

The first term in equation 3.16 describes the friction force caused by relative ion-electron fluid motion and determines the electrical conductivity of the plasma. As temperature increases the electrical conductivity decreases, which is equivalent to the rate of Coulomb collisions decreasing [22]. Thus, the electrical current is carried by the electrons in the high-velocity tail of the Maxwellian distribution.

The smaller cross-section of hotter particles result in a *thermal force* considered in the second term of equation 3.16. Equation 3.17 represents the thermal energy transferred between electrons and ions due to thermally-equilibrating Coulomb collisions, and is correspondingly subtracted from equation 3.18. The second term of equation 3.18 is the *Ohmic heating* of the electrons, and the third term represents the work done against the thermal force.

3.2 The multifluid code package UEDGE

UEDGE is a two-dimensional multifluid transport code for collisional edge plasmas capable of simulating curvilinear geometries, such as actual tokamak geometries that conform to shaped divertor surfaces [32]. UEDGE solves the fluid equations on two-dimensional mesh grid. The curvilinear mesh is generated based on the poloidal flux surface from MHD codes such as EFIT [33]. The physics equations solved have been developed from the B2 equations of

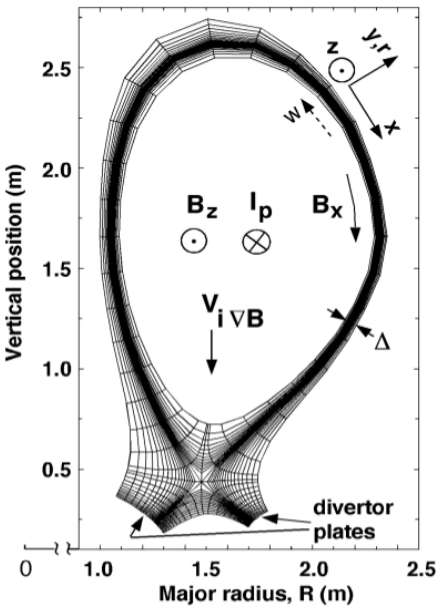

Figure 3.1: Single-null UEDGE geometry of the simulated region, showing the coordinates used and the magnetic field components. The plasma current I_p generates the poloidal field B_x and the vector $\mathbf{w}$ is the bi-normal direction $\hat{\mathbf{i}}_{\|} \times \hat{\mathbf{y}}$ [7].

Braams [34], which in turn are modified Braginskii equations with *ad hoc* radial diffusion coefficients simulating anomalous turbulent cross-field (radial) transport and volumetric sources and sinks associated with interactions with neutral gas components. The diffusive/convective approximation of the turbulent radial transport has been adopted due to the limited understanding of plasma micro-turbulence, and should be verified against experimental measurements or dedicated, kinetic simulations. Typically, only the diffusive model is used. Parallel transport approximated classically with imposed *flux limits* addressing kinetic effects [35]. UEDGE is capable of simulating an arbitrary number of impurity species in addition to the plasma species. The hydrogen atom gas is described by a detailed fluid model with a parallel momentum equation. UEDGE is capable of calculating the electrostatic potential with drift effects and electrical currents, and solves the equations using a fully-implicit, modified Newton iteration [36, 37].

3.2.1 The UEDGE equations

The basic UEDGE equations are given in [7], where the variable **u** denotes the total velocity while the variable **v** is used for the classical velocity terms. The total velocity, **u** can be split into the components u_x and u_y, where the subscripts x and y refer to the poloidal and radial (cross-field) directions, respectively (Fig. 3.1). The parallel (to the magnetic field lines) velocity $u_\parallel$ is taken to be classical: $u_\parallel = v_\parallel$. Here, subscript $\parallel$ refers to the parallel direction. The classical components of the parallel velocity are denoted v and differ by the anomalous diffusive term. The poloidal and radial components of the parallel velocity are

$$u_{x,i} = \frac{B_x}{B} v_{\parallel i} + v_{\mathbf{E}\times\mathbf{B},x} + v_{\nabla B,x}, \tag{3.19}$$

$$u_{y,i} = -\frac{D_\perp}{n_i}\frac{\partial n_i}{\partial y} + V_\perp + v_{\mathbf{E}\times\mathbf{B},y} + v_{visc,y,i}. \tag{3.20}$$

Here, $v_{\mathbf{E}\times\mathbf{B},k}$ is the $\mathbf{E}\times\mathbf{B}$-drift in k-direction, $v_{\nabla B,k}$ the sum of the curvature and grad-B drifts in k-direction (chapter 2), and B_x the magnetic field strength in the poloidal direction. $D_\perp$ and $V_\perp$ are the anomalous cross-field (radial) transport coefficients characterizing radial transport, which is assumed to be ambipolar. The last term in equation 3.20 describes the non-ambipolar viscous drift which connects the electrostatic potential on adjacent flux surfaces [38]. The electron velocities are of the same form as the ion velocities presented above, except that the electron radial velocity does not consider the viscous drift owing to their comparatively small gyroradii.

3.2.1.1 The continuity equation

The ion continuity equation solved in UEDGE is

$$\frac{\partial}{\partial t} n_i + \frac{1}{\sqrt{g}}\frac{\partial}{\partial x}\left(\frac{\sqrt{g}}{h_x} n_i u_{x,i}\right) + \frac{1}{\sqrt{g}}\frac{\partial}{\partial y}\left(\frac{\sqrt{g}}{h_x} n_i u_{y,i}\right) = \nu_i n_a - \nu_r n_i, \tag{3.21}$$

where $\nu_i = n_e\langle\sigma_i v_e\rangle$ and $\nu_r = n_e\langle\sigma_r v_e\rangle$ are the ionization and recombination frequencies, respectively. UEDGE considers atomic processes through temperature and density-dependent *reaction rates* ($\langle\sigma_r v_e\rangle = [\mathrm{m^3 s^{-1}}]$). Such reaction rates are a description of atomic processes, and retrieved from databases such as ADAS [39] and AMJUEL [40]. These reaction rates are discussed in section 4. The metric coefficients $h_x \equiv 1/||\nabla x||$, $h_y \equiv 1/||\nabla y||$, and $\sqrt{g} = 2\pi R h_x h_y$ in equation 3.21 describe the curvature and nonuniformity of the cells composing the numerical domain and are henceforth omitted for

clarity. All divergence operators in the following equations should have these terms added.

The time-derivative describes the time-dependent change in density caused by the various plasma processes in each cell, and is zero at steady-state. The remaining LHS terms describes the particle fluxes in the poloidal and radial directions, respectively, and the RHS terms consider volumetric recombination sinks and ionization sources, respectively. The current UEDGE model considers EIR and charge exchange recombination processes.

Equation 3.21 is solved separately for each ion species included in the simulation, and the electron density follows from the quasineutrality assumption.

3.2.1.2 The momentum equation

The ion parallel momentum equation solved in UEDGE is

$$\begin{aligned}\frac{\partial}{\partial t}(m_i n_i v_{\parallel i}) + \frac{\partial}{\partial x}\left(m_i n_i v_{\parallel i} u_{x,i} - \eta_{x,i}\frac{\partial v_{\parallel i}}{\partial x}\right) \\ + \frac{\partial}{\partial y}\left(m_i n_i v_{\parallel i} u_{y,i} - \eta_{y,i}\frac{\partial v_{\parallel i}}{\partial y}\right) = \frac{B_x}{B}\left(-\frac{\partial P}{\partial x}\right) \\ - n_a \nu_{CX}(m_i v_{\parallel i} - m_a v_{\parallel a}) + m_a n_a \nu_i v_{\parallel a} - n_i \nu_r m_i v_{\parallel i}, \qquad (3.22)\end{aligned}$$

where $\eta_{x,i} = (B_x/B)^2\eta_\parallel$ is the classical viscosity, $\eta_{y,i} = m_i n \Upsilon_{\parallel a}$ the anomalous radial viscosity, $P = p_e + p_i$ the total plasma pressure, $\nu_{CX} = n_i\langle\sigma_{CX} v_i\rangle$ is the ion-atom charge-exchange frequency, and the subscript a refers to neutral hydrogen atoms. The $m_i n_i v_{\parallel,i} u_{x,i}$-term describes the momentum flow in the poloidal direction, and the η-terms refer to the *viscous stress* of the fluid, also referred to as the *momentum diffusion*. Applying pressure in the direction of the fluid will cause momentum diffusion in the direction of the applied pressure. The fluid equations consider the pressure conservation along each flux tube and, thus, the momentum distribution by pressure is considered through the $\eta_{xi}\partial v_{\parallel,i}/\partial x$-term. In the radial direction the plasma can be flowing at different velocities in each flux-tube in what is considered to be *laminar flow*. The fluid friction between adjacent flux tubes, or *shear stress*, decelerates the faster flowing plasma and accelerates the slower flowing plasma, resulting in radial diffusive momentum transfer described by $\eta_{y,i}\partial v_{\parallel,i}/\partial y$. The $m_i n_i v_{\parallel i} u_{y,i}$-term describes the radial convection of parallel momentum between adjacent flux tubes.

The RHS terms of equation 3.22 describe the momentum sinks and sources considered in UEDGE. Ion-atom friction is mediated by CX reactions and transfers momentum between hydrogen ions and atoms at a rate $n_a\nu_{CX}(m_i v_{\parallel i} - m_a v_{\parallel a})$, which is dependent on the relative velocity of the hydrogen ion and

atom fluids. The last RHS terms describe the momentum gain and loss by ionization and recombination since these processes change the mass and velocity of the fluid species. The static pressure exerted by the plasma (p_i) is analogous to directional momentum and is included in the total pressure term $P = p_e + p_i$.

Equation 3.22 is analogous to the Braginskii ion momentum equation (eq. 3.10) with the addition on RHS momentum recombination sinks and ionization sources, and a coupling to the atomic hydrogen momentum equation through ion-atom friction. Additionally, the inertialess electron momentum derived from equation 3.7,

$$\mathbf{F} - \nabla \boldsymbol{\pi}_e - \nabla P_e + e n_e (\mathbf{E} + \mathbf{V}_e \times \mathbf{B}) = 0 \tag{3.23}$$

has been used to eliminate the electric field and viscous contributions. Here, $\mathbf{F}$ is given by equation 3.16. Applying equation 3.23 results in the electron pressure (p_e) contribution to the total plasma pressure P through which the electron momentum contribution is considered.

3.2.1.3 The energy equations

The electron energy equation is

$$\begin{aligned}\frac{\partial}{\partial t}\left(\frac{3}{2} n_e T_e\right) + \frac{\partial}{\partial x}\left[C_{x,e} n_e u_{x,e} T_e - \kappa_{x,e}\frac{\partial T_e}{\partial x} - 0.71 n_e T_e \frac{B_x}{B}\frac{J_\parallel}{e n_e}\right] \\ + \frac{\partial}{\partial y}\left[C_{y,e} n_e u_{y,e} T_e - \kappa_{y,e}\frac{\partial T_e}{\partial y}\right] = \mathbf{j}\cdot\mathbf{E} \\ + \sum_\alpha \frac{\mathbf{j}_\alpha}{e n_e}\cdot\left(\nabla_\parallel p_e - \nabla_\perp \sum_\alpha p_\alpha\right) \\ - \nu_{eq}(T_e - T_i) + S_{Ee},\end{aligned} \tag{3.24}$$

where $\kappa_{x,j} = (B_x/B)^2 \kappa_{\parallel j}$ the classical heat conductivity, $\kappa_{y,j} = n\chi_j$ the anomalous radial heat conductivity, $C_{xj,yj}$ the convection coefficients, ν_{eq} the aforementioned rate of Coulomb energy exchange collisions, $j_\parallel$ the parallel current (section. 3.2.1.4), and j_α the component of ion all ion species α to the total current ($j_\alpha \equiv Z_\alpha e n_\alpha \mathbf{V}_\alpha$). Thus, $\sum_\alpha \mathbf{j}_\alpha = \mathbf{j} + e n_e \mathbf{V}_e$ where $\mathbf{j}$ is the total current.

The first and second square brackets on the LHS of equation 3.24 are the *heat fluxes* $Q_{qx,e}$ and $Q_{qy,e}$, respectively. The first term and second terms of the heat fluxes are the convected and conducted heat fluxes, respectively, in the appropriate direction. Here, the second terms is analogous to the Spitzer-Härm heat conductivity.

The first term of the RHS is the Ohmic heating term. This form of equation 3.24 is derived by using the inertial electron momentum equation and the pressure-balance equation $\mathbf{J} \times \mathbf{B} = \nabla_\perp(p_e + \sum_\alpha p_\alpha)$. The second RHS term, where $\sum_\alpha(\mathbf{j}_\alpha/en_e)$ describes the ion flow, also results from this derivation and describes the energy change by the pressure-gradient force. The third term describes ion-electron thermal equipartition which transfers energy between ions and electrons and is offset by the same term of opposite sign in the ion energy equation (eq. 3.25). The S_{Ee}-term represents volumetric sinks and sources, especially radiation and the dissociation energy, which are electron energy sinks. UEDGE computes Ly-α radiation to occur at regions of high ionization rates due to the excitation frequencies being high at such conditions.

The ion energy equation is

$$\begin{aligned}\frac{\partial}{\partial t}\left(\frac{3}{2}n_iT_i\right) + \frac{\partial}{\partial x}\left(\left[C_{x,i}n_iu_{x,i}T_i - \kappa_{x,i}\frac{\partial T_i}{\partial x}\right] - \eta_{x,i}\frac{\partial v_{\|i}}{\partial x}\right) \\ + \frac{\partial}{\partial y}\left(\left[C_{y,i}n_iu_{y,i}T_i - \kappa_{y,i}\frac{\partial T_i}{\partial y}\right] - \eta_{y,i}\frac{\partial v_{\|i}}{\partial y}\right) = \mathbf{u}\cdot\nabla p_i \\ + \nu_{eq}(T_e - T_i) + K_{eq,g}(T_a - T_i) \\ + K_{eq,im}(T_m - T_i) + \frac{1}{2}m_iv_{\|i}^2n_i\nu_i - \frac{1}{2}m_iv_{\|i}^2n_i\nu_r + S_{Ei}, \quad (3.25)\end{aligned}$$

with $\eta_{x,y}$, $\kappa_{x,y}$, ν_i, ν_r, κ_i, and $C_{x,y}$ as described above and subscripts a and m refer to the atomic and molecular species, respectively. The terms in square brackets are ion heat fluxes in respective directions ($Q_{x,i}$ and $Q_{y,i}$), analogous to the electron heat fluxes.

The viscous contributions in the second and third LHS terms are viscous heating of the ion fluid due to pressure and fluid shear, respectively. The viscous terms are omitted from the electron energy equation (eq. 3.24) due to the small inertia of electrons compared to the ions. The first term on the RHS describes energy transfer by the pressure-gradient force and the second term is the thermal equipartition energy between ions and electrons, which is offset by the same term of opposite sign in the electron energy equation. The third term describes the ion-atom energy exchange which is dominated by the large volumetric CX rate ($K_{eq,a} \approx m_in_a\nu_{CX}$) resulting in $T_a = T_i$, with the same term of opposite sign considered in the atom energy equation. Here, the $K_{eq,m}(T_m - T_i)$-term describes the non-resonant, elastic scattering energy exchange events between ions and molecules, with the same term of opposite sign being considered in the molecular energy equation. This term is only considered when the molecular energy equation is solved. The $\frac{1}{2}m_iv_{\|,i}^2n_i\nu$-terms describe ion ionization sources and recombination sinks.

For Maxwellian species these terms are given by $\frac{1}{2}T_a n_i \nu_i$ and $\frac{1}{2}T_i n_i \nu_r$, respectively, with the same terms of opposite signs considered in the atom energy equation. S_{Ei} are other volumetric ion energy sinks and sources, such as *neutral beam injection* (NBI) and *radio-frequency* (RF) heating.

3.2.1.4 The potential equation

By assuming quasineutrality, and taking the difference of the ion and electron continuity equations the plasma potential (ϕ) equation is derived:

$$\nabla \cdot \mathbf{J}(\phi) = \frac{\partial}{\partial x} J_x + \frac{\partial}{\partial y} J_y, \tag{3.26}$$

The current considered in equation 3.26 excludes the magnetization current and is

$$\mathbf{J} = \left[n_e e(\mathbf{v}_{i,\nabla B} - \mathbf{v}_{e,\nabla B}) \cdot \hat{\mathbf{x}} + J_{\parallel} \frac{B_x}{B} \right] \hat{\mathbf{x}} + n_e (v_i - v_e) \hat{\mathbf{y}}, \tag{3.27}$$

where $n_e e(\mathbf{v}_{i,\nabla B} - \mathbf{v}_{e,\nabla B}) \cdot \hat{\mathbf{x}}$ is independent of ϕ and acts as a source term in equation 3.26. In equation 3.27, $J_{\parallel}$ is derived from the inertialess electron momentum equation:

$$J_{\parallel} = \frac{e n_e}{0.51 m_e \nu_{ee}} \frac{B_x}{B} \left(\frac{1}{n_e} \frac{\partial p_e}{\partial x} - e \frac{\partial \phi}{\partial x} + 0.71 \frac{\partial T_e}{\partial x} \right), \tag{3.28}$$

where ν_{ee} refers to the electron self-collisionality frequency [22].

3.2.1.5 The UEDGE fluid neutral model of hydrogen atoms

The fluid neutral model utilized in UEDGE for modeling hydrogen atoms assumes the atoms to be an inertial fluid. The equations solved for hydrogen atoms are presented below, starting from the atom continuity equation

$$\frac{\partial}{\partial t} n_a + \frac{\partial}{\partial x}(n_a v_{x,a}) + \frac{\partial}{\partial y}(n_a v_{y,a}) = -\nu_i n_a + \nu_r n_i + \nu_d n_m. \tag{3.29}$$

Here, the RHS atom source and sink terms correspond to the sink and source terms, respectively, in the ion continuity equation (eq. 3.21) and $\nu_d = n_e \langle \sigma_d v_m \rangle$ is the hydrogen atom source due to dissociation of molecules (eq. 3.34). UEDGE assumes each molecule to dissociate into two hydrogen atoms, thus, molecular ions are not considered here. A corresponding equation is solved for impurity atoms, without considering dissociation since impurity molecules are not considered in the model.

The parallel momentum equation solved for the hydrogen atoms is

$$\begin{aligned}\frac{\partial}{\partial t}(m_a n_a v_{\parallel a}) + \frac{\partial}{\partial x}\left(m_a n_a v_{\parallel a} u_{gx,a} - \eta_{x,a}\frac{\partial v_{\parallel a}}{\partial x}\right) \\ + \frac{\partial}{\partial y}\left(m_a n_a v_{\parallel i} u_{y,a} - \eta_{y,a}\frac{\partial v_{\parallel a}}{\partial y}\right) = \frac{B_x}{B}\left(-\frac{\partial p_a}{\partial x}\right) \\ + n_a \nu_{CX}(m_i v_{\parallel i} - m_a v_{\parallel g}) - m_a n_a \nu_i v_{\parallel a} + n_i \nu_r m_i v_{\parallel i}, \qquad (3.30)\end{aligned}$$

where the viscous coefficients $\eta_a \approx m_a n_a Ta/(m_a \nu_{el,a})$ are determined by the elastic collision scattering frequency with other particles, $\nu_{el,a}$. The pressure-driven momentum transport is analogous to that of the ion momentum equation and the remaining RHS terms are sinks and sources corresponding to the sources and sinks, respectively, of the ion momentum equation (eq. 3.22).

The inertial and viscous terms in equation 3.30 can be neglected by assuming subsonic parallel-**B** atom velocities, resulting in a simple expression for perpendicular velocity:

$$\mathbf{v}_{\perp a} = \mathbf{v}_{\perp i} - \frac{\nabla_\perp (n_a T_a)}{m_a n_a \nu_{CX}}. \qquad (3.31)$$

The neutral atom energy equation is

$$\begin{aligned}\frac{\partial}{\partial t}\left(\frac{3}{2} n_a T_a\right) + \frac{\partial}{\partial x}\left(\left[C_{x,a} n_a u_{x,a} T_a - \kappa_{x,a}\frac{\partial T_a}{\partial x}\right] - \eta_{x,a}\frac{\partial v_{\parallel a}}{\partial x}\right) \\ + \frac{\partial}{\partial y}\left(\left[C_{y,a} n_a u_{y,a} T_a - \kappa_{y,a}\frac{\partial T_a}{\partial y}\right] - \eta_{y,a}\frac{\partial v_{\parallel a}}{\partial y}\right) = \mathbf{u}\cdot\nabla p_a \\ + K_{eq,a}(T_i - T_a) + K_{eq,am}(T_m - T_a) \\ - \frac{1}{2} m_i v_{\parallel i}^2 n_i \nu_i + \frac{1}{2} m_i v_{\parallel i}^2 n_i \nu_r + S_{Ea}, \qquad (3.32)\end{aligned}$$

where the atom thermal conductivity terms are given by $\kappa_a \approx n_a T_a/(m_a \nu_{el})$ analogous to the gaseous viscosity. The $K_{eq,am}(T_m - T_a)$-term describes elastic energy-exchange collisions between atoms and molecules, where $K_{eq,am}$ is the volumetric atom-molecule energy transfer rate and is included in the molecular temperature equation with opposite sign. This term is only considered when the molecular energy equation is solved. The S_{Ea}-term describes volumetric sources and sinks, such as the dissociation source of Franck-Condon energy. The remaining terms are analogous to those in equation 3.25.

Coupled codes, such as SOLPS [4] or EDGE2D-EIRENE [5, 6] treat the neutral species as kinetic particles. The particle trajectories of a test particle population, and interactions with the plasma background and possibly a fluid neutral background deduced from the test particles, are simulated. Based on

the kinetic distribution of the ensemble, statistical estimates of the fluid quantities on the kinetic solver (EIRENE) grid can be made. The fluid quantities are then interpolated to the fluid solver grid and the neutral fluid quantities used for a number of fluid solver iterations, after which the kinetic neutrals are simulated again. This results in no numerical convergence of such codes and a demand for significant computational power. In contrast, full fluid models, such as the one utilized in UEDGE, reach numerical convergence where the sum of all terms in the equations balance to $\sim 10^{-10}$ in steady-state compared to individual terms of order unity. The omission of kinetic effects can be alleviated by imposing flux limits in the parallel direction and considering plasmas of sufficient collisionality.

Because UEDGE assumes strong CX coupling between hydrogen ions and atoms, resulting in $T_a \approx T_i$, the ion and atom energy equations are solved together:

$$\begin{aligned}
&\frac{\partial}{\partial t}\left(\frac{3}{2}(n_i + n_a)T_{ia}\right) \\
&+ \frac{\partial}{\partial x}\left(C_{x,ia}(n_i u_{x,i} + n_a u_{x,a})T_{ia} - (\kappa_{x,i} + \kappa_{x,a})\frac{\partial T_{ia}}{\partial x} - \eta_{x,i}\frac{\partial v_{\|i}}{\partial x} - \eta_{x,a}\frac{\partial v_{\|a}}{\partial x}\right) \\
&+ \frac{\partial}{\partial y}\left(\left[C_{y,ia}(n_i u_{y,i} + n_a u_{y,a})T_{ia} - (\kappa_{y,i} + \kappa_{y,a})\frac{\partial T_{ia}}{\partial y}\right] - \eta_{y,i}\frac{\partial v_{\|i}}{\partial y} - \eta_{y,a}\frac{\partial v_{\|a}}{\partial y}\right) \\
&= \mathbf{u}_i \cdot \nabla p_i + \mathbf{u}_a \cdot \nabla p_a + \nu_{eq}(T_e - T_i) \\
&+ (K_{eq,am} + K_{eq,im})(T_m - T_{ia}) + (S_{Ea} + S_{Ei}),
\end{aligned} \tag{3.33}$$

where the ia subscript signifies the mean of the ion and atom values. Although the CX-coupling between the ion and atom parallel momentum equations is strong, the parallel momentum equations are solved separately. This is due to the ions being subject to the Bohm-condition at the sheath edge, while the velocity of the neutral atoms is not affected by the electrostatic potential of the sheath.

3.2.1.6 UEDGE molecular hydrogen model

The UEDGE molecular model does not consider volume recombination of molecules, molecular ions (D_2^+), vibrationally excited molecules, or radiative molecular processes and assumes the only molecular source to be ion and atom recycling as molecules at the target plates. Thus, the continuity equation takes the form

$$\frac{\partial}{\partial t}n_m + \frac{\partial}{\partial x}(n_m v_{x,m}) + \frac{\partial}{\partial y}(n_m v_{y,m}) = -\nu_d n_m, \tag{3.34}$$

where the RHS describes the molecular sink due to dissociation. The molecules are assumed diffusive with subsonic flow velocities, resulting in the expression for velocity

$$\mathbf{v}_m = -\frac{1}{m_m n_m}\frac{\nabla p_m}{\nu_{ela}+\nu_{eli}} + \frac{\nu_{ela}}{\nu_{ela}+\nu_{eli}}\mathbf{v}_a + \frac{\nu_{eli}}{\nu_{ela}+\nu_{eli}}\mathbf{v}_i. \tag{3.35}$$

Here, the first term describes molecular velocities due to the pressure-gradient force and the latter terms describes the conformity of the molecular velocity to the atom and ion velocities, respectively. The balance of the species contribution and the pressure-gradient force is determined by the strength of the elastic collisions: the stronger the elastic collisions, the more dominated by the ions and atoms the molecular velocity becomes.

The basic molecular model uses constant, user-defined molecular temperatures on the UEDGE grid, which means the model is not self-consistent with respect to energy. In order to better describe molecular processes in the plasma a molecular energy equation is implemented according to

$$\begin{aligned}\frac{\partial}{\partial t}\left(\frac{3}{2}n_m T_m\right) + \frac{\partial}{\partial x}\left(\left[C_{x,m}n_m u_{m,i}T_m - \kappa_{x,m}\frac{\partial T_m}{\partial x}\right] - \eta_{x,m}\frac{\partial v_{\|m}}{\partial x}\right) \\ + \frac{\partial}{\partial y}\left(\left[C_{y,m}n_m u_{y,m}T_m - \kappa_{y,m}\frac{\partial T_m}{\partial y}\right] - \eta_{y,m}\frac{\partial v_{\|m}}{\partial y}\right) \qquad (3.36)\\ = K_{eq,im}(T_i - T_m) + K_{eq,gm}(T_a - T_m) + S_{Em}. \qquad (3.37)\end{aligned}$$

Here, S_{Em} represent volumetric molecular power sources and sinks, such as the dissociative energy sink. The remaining terms are defined analogously to the corresponding atomic and ionic terms terms (eqs. 3.30,3.32, and 3.25). The molecular energy equation has been implemented in UEDGE, but is still being verified at the time of writing of this thesis.

The UEDGE molecular model does not take into account MAR, facilitated by rovibrational molecules, and only considers neutral molecules. Each molecule is dissociated into two atoms with the Franck-Condon energy by an electron. Thus, UEDGE does not consider a number of molecular dissociation and recombination processes [40], which might affect the plasma predictions.

3.2.1.7 A simplified impurity model in UEDGE

The impurity gas continuity is modeled by continuity equations analogous to the ion and atom continuity equations (eq. 3.21 and 3.29), and the impurity temperature is taken to be the common ion temperature. The ion gas is modeled by a the diffusion equation where the diffusion coefficient is taken

to be

$$D_z = \frac{T_z}{m_z \left(\nu_{CX,zi} + \nu_{CX,z} + \frac{16 m_i}{3(m_z+m_i)} (\nu_{el,zi} + \nu_{za} + \nu_{zz}) \right)}, \tag{3.38}$$

where subscript z refers to the impurity ions of charge Z, $\nu_{CX,zi}$ to the CX frequency between hydrogen and the impurity ion, and $\nu_{CX,z}$ to CX between impurity atoms and ion species z. The factor of the last term describes the elastic collision of impurity ions with hydrogen ions, atoms, and impurity ions.

UEDGE can include impurity ions at the same level as the hydrogen ion equations given above, including ionization and recombination between charge states, interspecies friction, and thermal forces. However, for trace-level impurities (small density compared to hydrogen), it is efficient to consider a reduction on the impurity parallel momentum equations. This force-balance model neglects inertial effects in the parallel momentum equation in comparison to forces from pressure-gradient, thermal force, electric-field force, and friction with hydrogen ions as follows:

$$\begin{aligned} &\frac{B_x}{B} \left[-\frac{\partial p_z}{\partial x} + \alpha_z n_z \frac{\partial T_e}{\partial x} + \beta_z n_z \frac{\partial T_i}{\partial x} - Z e n_Z \frac{\partial \phi}{\partial x} \right] \\ &\quad = (u_{\parallel z} - u_{\parallel i}) m_i n_i \nu_{iz}, \end{aligned} \tag{3.39}$$

where α_z and β_z are defined in [41, 42, 7]. The first term in the square brackets is the impurity pressure gradient force, the second and third the electron and ion thermal forces, respectively. The last LHS term is the electrostatic force in the SOL and the RHS describes the friction force of the ions with other plasma species.

3.2.1.8 UEDGE boundary conditions

UEDGE has options for various sets of boundary conditions for tailoring of simulations which are described in detail in [7]. This section outlines the boundary conditions used within this work.

The core boundary conditions for ion and electron energy equations and ion density are the primary independent variables of the UEDGE simulations. The ion density at the core boundary, which is located well inside of the separatrix, is uniform and user defined. The electron density follows from the impurity core boundary condition (below) through the quasineutrality condition. The energy boundary conditions at the core are specified by constant electron and ion power across the core boundary distributed uniformly along the separatrix.

The ion parallel velocity boundary conditions are the Bohm sheath conditions of the plasma reaching sonic speed at the divertor plates, allowing for supersonic parallel velocities, if the solution seeks such a state. The inner and outer wall parallel velocity boundary conditions are *slip boundary conditions*, $\mathrm{d}u_{\parallel}/\mathrm{d}y = 0$. Slip boundary conditions are also used for imposing parallel velocity at the core boundary.

The energy equations, including the energy drift energy, have plate boundary conditions set by the energy transmission factors for electrons and ions according to $Q_{qx,e} = \gamma_e T_e \Gamma_{x,e}$ and $Q_{qx,i} = \gamma_i T_i \Gamma_{x,i}$, respectively, where Q_q is the poloidal heat flux. The model used computes the sheath potential contribution to the electron energy transmission factors γ_e from the solution using sheath conditions consistent with the parallel current at the plates. The kinetic energy contributions to γ_e and γ_i are 2 and 2.5 for electrons and ions, respectively. The radial boundary conditions for the ion and electron energy equations are limited by the radial temperature gradient scale-lengths.

The potential boundary conditions at the walls are given by Neumann boundary conditions ($\partial\phi/\partial y = 0$) in the radial direction. At the plates the potential has Dirichlet boundary conditions determined by the plate potentials and sheath potential gradient as evaluated by UEDGE. At the core the potential boundary condition is given by the second derivative of the potential in the radial direction being zero.

The impurity density boundary conditions are given by zero impurity atom particle flux over the boundary core and zero ion particle flux over the core boundary with poloidally constant core boundary density. Radial density gradient scale length boundary conditions are applied for the impurity ions, with the walls reflecting the impurity atoms and absorbing all incoming ions. In the parallel direction the impurity velocity is determined by the force-balance equation, the plates reflect all incoming impurity atoms and absorb all incoming impurity ions. The impurity sources are chemical sputtering from deuterium ions and atoms according to the Haasz 1997 model with low-energy corrections [7] and physical sputtering from deuterium ions and atoms at the plates. At the PFR and SOL grid boundaries ion chemical and physical sputtering is considered.

UEDGE allows for user-defined gas puffing at the walls or gas densities at the core boundary. Here, uniform gas densities of 2×10^{13} m^{-3} have been set at the core boundary. The hydrogen ion flux incident on the plates and walls are recycled as hydrogen atoms according to $\Gamma_a = -\varepsilon_{rec}\Gamma_i$ where ε_{rec} is the recycling coefficient. Pumping is represented by wall and plate *albedos* (α) which can be set to pump atoms and molecules locally at different rates, $1-\alpha$, or uniformly. When molecules are included, PFR and SOL grid boundaries and plates act as the single molecular source where $\Gamma_m = -(1/2)\,(\Gamma_i + \Gamma_a)$

and $\varepsilon_{rec} \in (-1, 0)$ acts as albedo. Hydrogen atoms and molecules have Neumann boundary conditions ($\partial/\partial y = 0$) in the radial direction at the walls.

Chapter 4

Implementation

4.1 UEDGE case setup

This work investigates UEDGE simulations of DIII-D shot 160299 and companions at higher densities, 160300-02. Experimentally, the plasmas constituted density scans in low-confinement mode to produce sheath-limited, high-recycling and detached conditions to study the SOL and validate edge fluid codes. The scans were performed at fixed plasma current (1.3 MA), toroidal magnetic field (2.1 T), and total (ohmic and neutral beam) input power (2.2 MW) in a configuration with the ion ∇B drift in the direction of the lower divertor. The experimental setup and results are described in [43] and [44].

The UEDGE simulations were performed on an EFIT MHD equilibrium dated December 10, 2013 corresponding to shot 160299 at 2230 ms (Fig. 4.1). The UEDGE simulations evaluate steady-state plasmas for input power $P_{in,i} = P_{in,e} = 0.45$ MW at core densities ranging between $n_{core} = 8 \times 10^{18} - 5.9 \times 10^{19}$ m^{-3} in increments of 10^{18} m^{-3}, depending on the neutral model. In these studies drifts were not included (no-drift simulations). The core densities were varied to the upper and lower density limits after which convergence was no longer achieved. The simulations were run in time-dependent mode using the standard UEDGE Krylov-Newton solver [7] until a steady state solution was obtained, and convergence assured by evaluating the solution at time step of 10^{20} s with small residuals. As a result the time derivatives of the above UEDGE equations goes to zero and the remaining terms can be considered rates constant in time at steady state.

Hydrogen atoms were included as inertial neutrals with recycling coefficient $\varepsilon_{rec} = 1$. When molecules were not included in the simulations (no-molecule simulations), hydrogen atoms were uniformly pumped at the targets

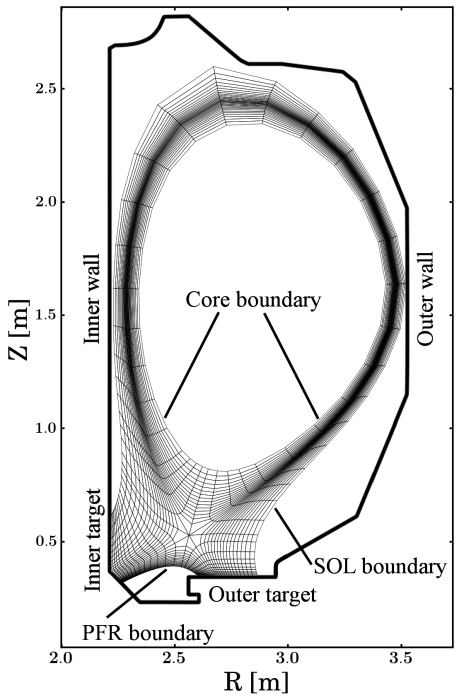

Figure 4.1: UEDGE MHD equilibrium used in this work.

at a 1% rate ($\alpha = 0.99$). The simulations considered carbon as the primary and only impurity species. The carbon ions were absorbed at the walls and plates ($\varepsilon_{rec} = 0$) and the carbon atoms were fully recycled ($\alpha = 1$), mimicking recycling of hydrocarbons CH_4. The dissociation energy per dissociated molecule is defined as 10 eV in the simulations. The Franck-Condon energy of each hydrogen atom is taken to be 2.5 eV per created atom, resulting in a 5 eV increase of the ion-atom fluid per dissociation reaction. The resulting difference of 5 eV is lost as dissociation radiation.

The density-dependent, carbon multi-charge state rates for ionization, recombination, radiation and CX used were ADAS B2 rates from SOLPS 5.0 compiled in February 2001. Temperature dependent log-log hydrogenic rates from Stotler at PPPL (95/07/10) [7] were used. The hydrogen rate coefficients used in the UEDGE simulations are presented in figure 4.2 together with the corresponding AMJUEL 2017 [40] and ADAS [39] rates. The ADAS rates used for ionization and recombination are metastable unresolved 2012 hydrogen rates and the CX rates are metastable unresolved 1996 deuterium rates. The UEDGE ionization and recombination rates are within 7% (20%) and 5% (8%) of the ADAS (AMJUEL) rates, respectively. Here, the difference between the UEDGE and ADAS ionization rates are the

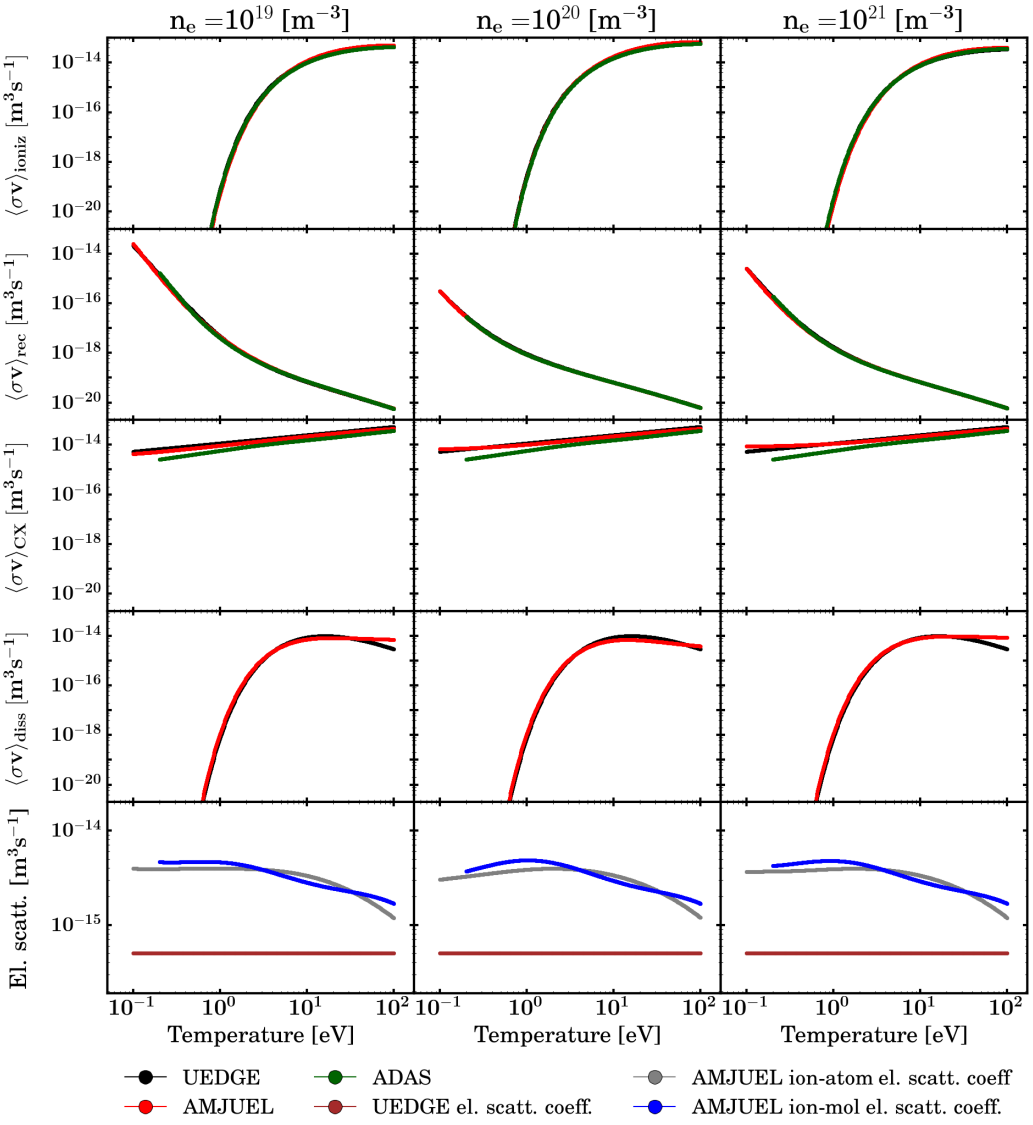

Figure 4.2: UEDGE (black) ionization, recombination, CX and dissociation rates as a function of temperature and electron densities of 10^{19} m^{-3} (left column), 10^{20} m^{-3} (middle column) and 10^{21} m^{-3} (right column) plotted together with the corresponding ADAS (green) and AMJUEL (red) rates. Note the logarithmic axes.

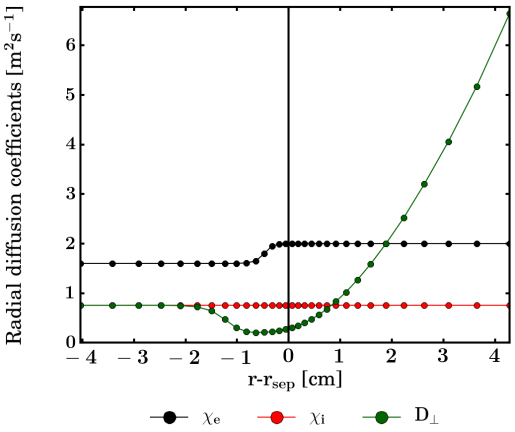

Figure 4.3: Assumed coefficients for anomalous radial thermal diffusion for the electrons (black) and the ions (red), and particle diffusivity (green) used in the UEDGE simulations. The radial profiles are plotted at the OMP.

largest at temperatures of ~ 30 eV and low densities ($n_e \approx 10^{18}$ m^{-3}). No ADAS dissociation or elastic scattering rates were available for the comparison. The UEDGE elastic scattering rates for ion-atom, ion-molecule, and molecule-atom elastic scattering are all equal to 5×10^{-16}. Note that the AMJUEL dissociation and elastic scattering rates are a function of temperature and the energy of one of the colliding particles (E) [40], here taken to be (left-to-right column) $E = 0.1$ eV, $E = 0.5$ eV, and $E = 1$ eV. The UEDGE rates used for CX are within 20% of the AMJUEL rates, but are a factor of ~ 3 higher than the ADAS rates at low temperatures. The elastic scattering rates used in UEDGE have no dependency on temperature and are approximately one order of magnitude smaller than the corresponding AMJUEL rates. The temperature dependent UEDGE dissociation rate is $\sim 30\%$ higher the the AMJUEL rates at temperatures around $T \approx 10$ eV and decreases more rapidly as the temperature increases and are 45% lower at $T \approx 100$ eV.

Above the X-point the radial particle and electron heat diffusivities were set to be radially varying according to figure 4.3. Below the X-point they are assumed spatially constant: $D_\perp = 1$ m^{2}s^{-1} and $\chi_e = 2$ m^{2}s^{-1}. Here, the radial ion thermal diffusivity was assumed to be constant in the whole domain: $\chi_i = 0.75$ m^{2}s^{-1} (Fig. 4.3). The global anomalous radial electric conductivity was set to 10^{-8} and the convective coefficients were taken to be 2.5. The anomalous radial viscosity coefficient was assumed to be $\Upsilon_{\|a} = 2.6$ m^{2}s^{-1}.

The flux limits imposed on the parallel transport were the parallel velocity

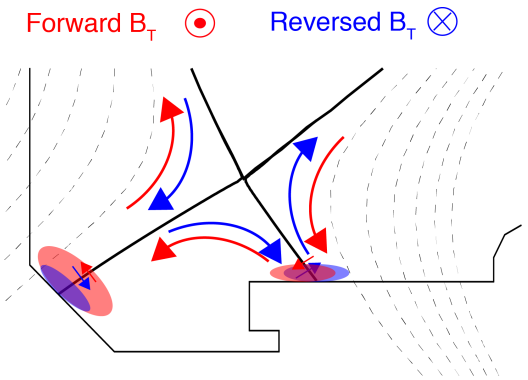

Figure 4.4: Schematic of ion drifts for forward (red) and reversed (blue) magnetic field directions in the divertor region of figure 4.1 [43].

flux limit ($\chi_{v_\parallel} = 1$), the parallel heat flux limit for electrons and ions ($\chi_{q\parallel,e} = 0.21$ and $\chi_{q\parallel,i} = 0.21$, respectively), the poloidal, radial and nonorthogonal gas diffusivity flux limits ($\chi_{x,D_g} = 1$, $\chi_{y,D_g} = 1$, and $\chi_{xy,D_g} = 1$, respectively), and the poloidal and radial gas temperature flux limits ($\chi_{x,T_g} = 1$ and $\chi_{y,T_g} = 1$, respectively).

The radial temperature gradient scale-lengths were set to 5 cm, for both hydrogen and impurity ions as well as for electrons, for the radial boundary condition of the energy equations. The ion densities were limited to at least 10^{16} m^{-3} and 10^{15} m^{-3} at the PFR and SOL grid boundary, respectively. The impurity ion densities were limited to at least 10^{7} m^{-3}.

These studies investigate the effect of molecules on the plasma solution. Thus, comparative UEDGE simulations with diffusive molecules of spatially constant temperature included have been performed (molecule simulations). When molecules were included, the hydrogen ion and atom fluxes incident on the plates were fully recycled as $\epsilon = 1$ and hydrogen molecules were removed by pumping at 1% rate ($\alpha = 0.99$). The molecular temperatures were defined to be $T_m = 0.025$ eV, $T_m = 0.1$ eV, $T_m = 0.5$ eV, and $T_m = 1$ eV.

Each set of data was evaluated with the ion ∇B drift direction towards the active X-point (forward B_T, Fig. 4.4). Configurations with the ion ∇B drift in the direction of the lower divertor typically result in divertor asymmetries, where the ion density builds up at the inner plate and in the peak ion density at the outer plate moves inside the PFR [43]. The $\mathbf{E} \times \mathbf{B}$-drifts are generally stronger than the ∇B-drifts since it scales as the inverse of the edge-plasma scale length while ∇B scales as the inverse of the major radius. The $\mathbf{E} \times \mathbf{B}$-drifts are responsible for the transport across the separatrix (section 3.2.1.4 and Fig. 4.4) [45].

Chapter 5

Results

5.1 Divertor detachment

The main parameters controlled in fusion experiments are the input power and density in the reactor, controlled by external heating and fueling, respectively. At constant input power the plasma density is the independent parameter required to compare experimental results and edge code predictions. The electron densities at the separatrix can be deduced from thermography using an infra-red camera (IRTV), bolometry and interferometry measurements in DIII-D. Thus, the electron separatrix density is the parameter used for comparison of code predictions and experimental results. Here, the separatrix electron density ($n_{e,sep}$) is taken in the first flux tube at the OMP. It is assumed that the electron separatrix density is representative of the upstream conditions, and any processes affecting the target plasma conditions are due to processes along the connection length. The outer target conditions have been analyzed, as the outer target is considered the critical location when considering plasma detachment. Alternatively, $T_{e,OSP}$ could be used.

The pressure rolls over at $\sim$28% lower separatrix densities ($n_{e,sep} \approx 1.3 \times 10^{19}$ m^{-3} and $n_{e,sep} \approx 1 \times 10^{19}$ m^{-3} no-molecule and molecule simulations, respectively) before the ion and electron temperatures reach temperatures typical for detachment ($T \approx 1$ eV): 2.3×10^{19} m^{-3} and 1.8×10^{19} m^{-3}, no-molecule and molecule simulations, respectively (Fig. 5.1). As volumetric power losses in the numerical domains increases at a close-to-linear rate with the separatrix density (Fig. 5.2a), the drop in target temperature is driven by the combined momentum and volumetric power losses. Increasing the molecular temperature shifts the pressure (Fig. 5.1a), temperature (Fig. 5.1b,c), current density (Fig. 5.1d) and power loss profiles (Fig. 5.2a)

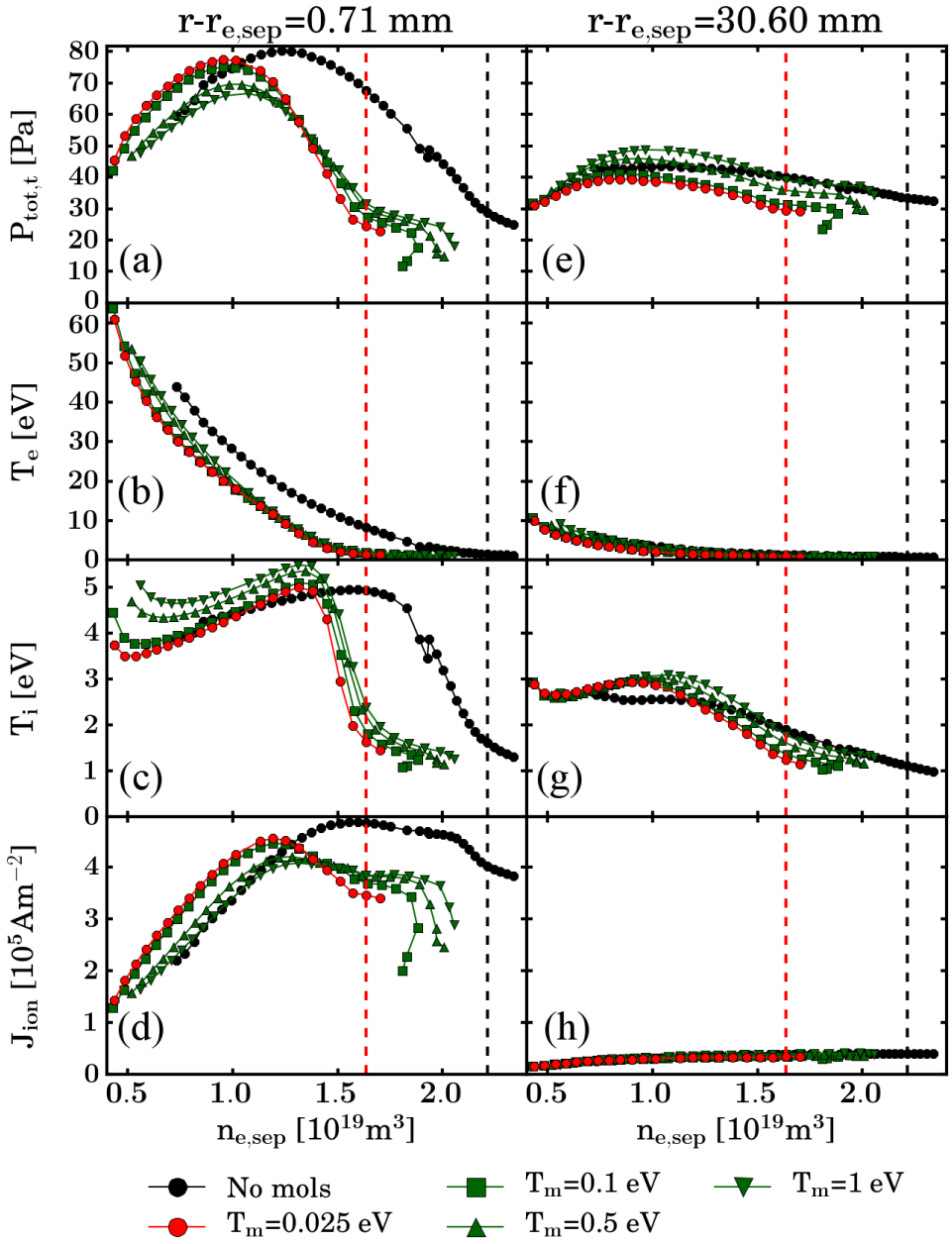

Figure 5.1: Plasma pressure (a,e), electron (b,f) and ion temperatures (c,g) and current density (d,h) in the near SOL (a–d) and far SOL (e–h) as a function of electron separatrix density. The dashed lines mark the separatrix densities for which $T_{e,peak,OT} < 1.5$ eV, considered as detached conditions, for the simulations with corresponding color. Here, the distances to the separatrix are mapped to the OMP and drifts are not included.

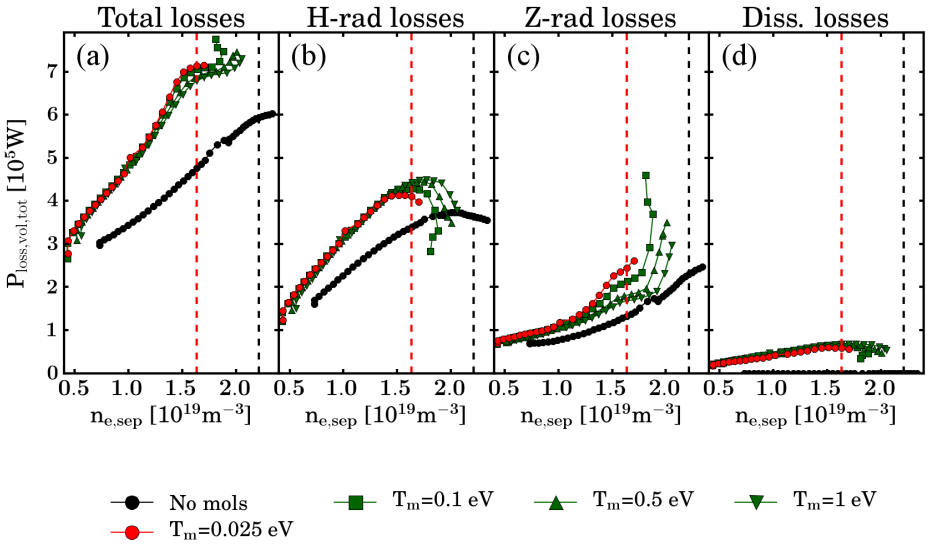

Figure 5.2: Total volumetric power losses (a) and hydrogen (b), impurity (c), and dissociation (d) contributions in the numerical domain as a function of electron separatrix density. The dashed lines mark the separatrix densities for which $T_{e,peak,OT} < 1.5$ eV, considered as detached conditions, for the simulations with corresponding color. Here, drifts are excluded.

to higher separatrix densities.

The total radiated power is 30% higher for the molecule simulations compared to the no-molecule simulations at $n_{e,sep} \approx 8 \times 10^{18}$ m^{-3}, and 55% higher at $n_{e,sep} \approx 1.6 \times 10^{19}$ m^{-3} (Fig. 5.2a). This increase is due to more hydrogen and impurity radiation at low separatrix densities and stronger increase in radiation with increasing separatrix density of the molecule simulations compared to the no-molecule simulations (Fig. 5.2b,c). The shape of the hydrogen radiation profile closely matches the peak outer target electron density (Fig. 5.3a). The relative shape of the hydrogen radiation and peak electron density curves have the same general shape, with an increase around $n_{e,sep} \approx 1.5 \times 10^{19}$ m^{-3} visible in both plots for the molecule simulations (Figs. 5.2c and 5.3a). The impurity radiation does not appear to match the peak target density curves, which is expected since carbon impurities radiate further up the divertor leg towards the X-point.

The peak electron and density profiles in the divertor have the same general shape for the no-molecule and molecule simulations, with the molecule simulation profiles shifted to lower densities (Fig. 5.3a). Here, the roll over in peak target electron density occurs at $n_{e,sep} \approx 1.7 \times 10^{19}$ m^{-3} for the molecule simulations, whereas in the no-molecule simulations, the peak target electron

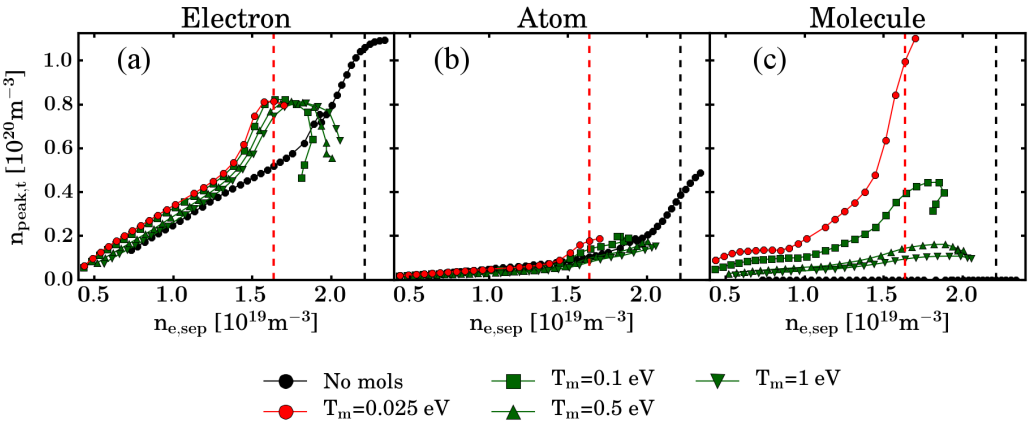

Figure 5.3: Peak target electron (a), deuterium atom (b) and molecule (c) densities as a function of separatrix density. The dashed lines mark the separatrix densities for which $T_{e,peak,OT} < 1.5$ eV, considered as detached conditions, for the simulations with corresponding color. Here, drifts are excluded.

density saturates at $n_{e,sep} \approx 2.4 \times 10^{19}$ m^{-3}. The peak target electron density profile of the no-molecule simulations indicates the electron density would roll over if the separatrix density would be increased further. The peak target atom density profiles are similar for the no-molecule and molecule simulations (Fig. 5.3b). The molecule densities dominate over the atomic densities and result in higher combined atom and molecule densities for the molecule simulations compared to the no-molecule simulations (Fig. 5.3c). The peak target molecular density increases at the same separatrix densities as the current density to the target plate rolls over for the molecular simulations with $T_m = 0.025$ eV (Fig. 5.3c and 5.4). As the molecular temperature is raised from 0.025 eV to 1 eV, the molecule densities decrease by up to an order of magnitude at high separatrix density.

The ion current density rolls over at similar separatrix densities as when the ions and electrons reach $T \approx 1$ eV (Figs. 5.1, 5.4). The roll over of ion current density indicates onset of detachment at separatrix densities of 1.5×10^{19} m^{-3} and 2.1×10^{19} m^{-3}, no-molecule and molecule simulations, respectively. However, since the ion current current in the far SOL is generally lower than at the separatrix by an order of magnitude and is not rolled over (Fig. 5.1e,h) the plasma is not considered fully detached. Here, increasing the molecular temperature from 0.025 eV to 1 eV increases the roll over in peak current density to 9% higher separatrix densities, consistent with figures 5.1 and 5.2.

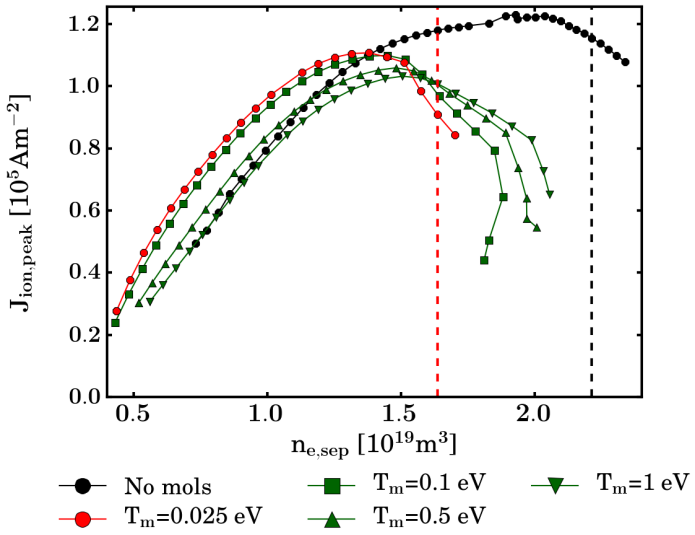

Figure 5.4: Peak current density to the outer divertor plate as a function of electron separatrix density. The peak current density profile is representative of the peak current profile. The dashed lines mark the separatrix densities for which $T_{e,peak,OT} < 1.5$ eV, considered as detached conditions, for the simulations with corresponding color. Here, drifts are excluded.

The perpendicular heat flux density incident on the outer target plate indicate that the outer divertor plasma is pronouncedly to fully detached at the highest separatrix densities (Fig. 5.5c). However, for the same separatrix densities the outer divertor plasma for the molecule simulations is pronouncedly detached at $n_{sep} \approx 1.5 \times 10^{19}$ m^{-3}, while the outer divertor plasma for the no-molecule simulations is partially detached (Fig. 5.5b). The peak perpendicular heat flux densities incident on the outer target and the peak position decrease monotonously and moves radially out from the separatrix, respectively, with increasing separatrix density (Fig. 5.5).

The volumetric power loss regions in the inner and outer divertor legs are found to expand upstream with stronger detachment (Fig. 5.6), in agreement with previous studies (section 2.4.4). Here, the molecule simulations with $T_m = 0.025$ eV are considered to be representative of the cases with higher molecular temperature. However, the spatial volumetric loss region contracts with increasing molecular temperature. The volumetric loss region detaches from the target plates together with the roll over in current density (Fig. 5.4). Hydrogen radiation is a factor of 1.4–3 and 7 higher than impurity radiation and dissociation losses (only present in the molecule simulations), respectively (Fig. 5.2). Thus, the volumetric losses in the no-drift

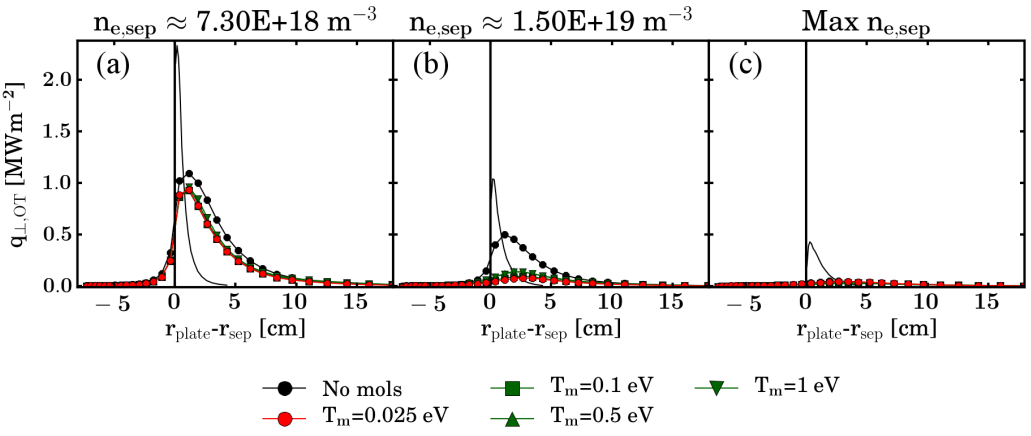

Figure 5.5: Profiles of perpendicular heat flux densities incident on the OT along the distance of the target plate for $n_{e,sep} \approx 7.3 \times 10^{18}$ m^{-3} (a), $n_{e,sep} \approx 1.5 \times 10^{19}$ m^{-3} (b), and the highest $n_{e,sep}$ for each setup (c). The vertical line marks the separatrix and negative $r_{plate} - r_{sep}$ values refer to the PFR. The black line is the upstream radial power profile. Here, and drifts are excluded.

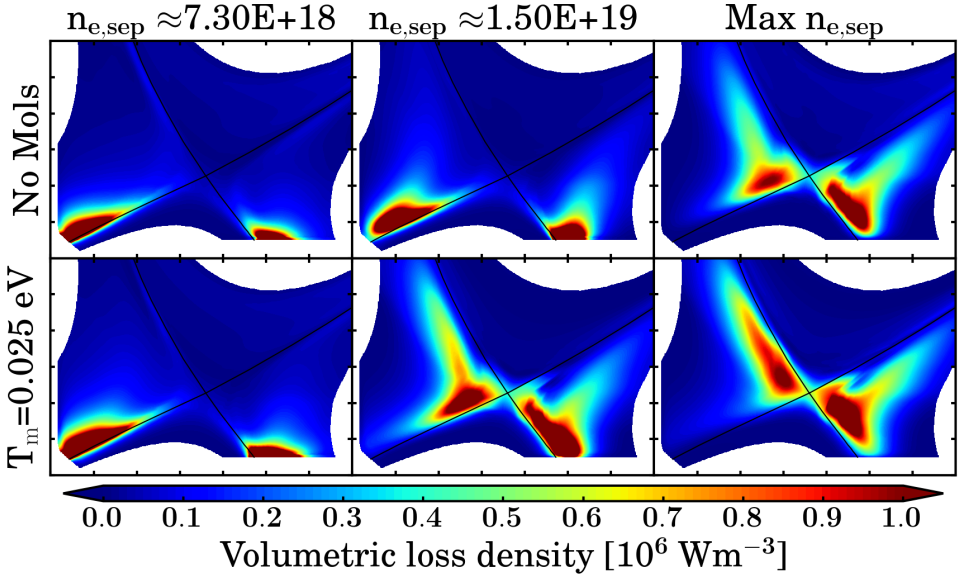

Figure 5.6: Poloidal profiles of the volumetric power loss density for the no-molecule (top row) and molecule (bottom row) simulations. The abscissa in each plot is the major radius, and the ordinate is the vertical distance with the black lines being the magnetic separatrix. Each column represents increasing separatrix density and the last column shows the maximum separatrix density for each model. Here, drifts are excluded.

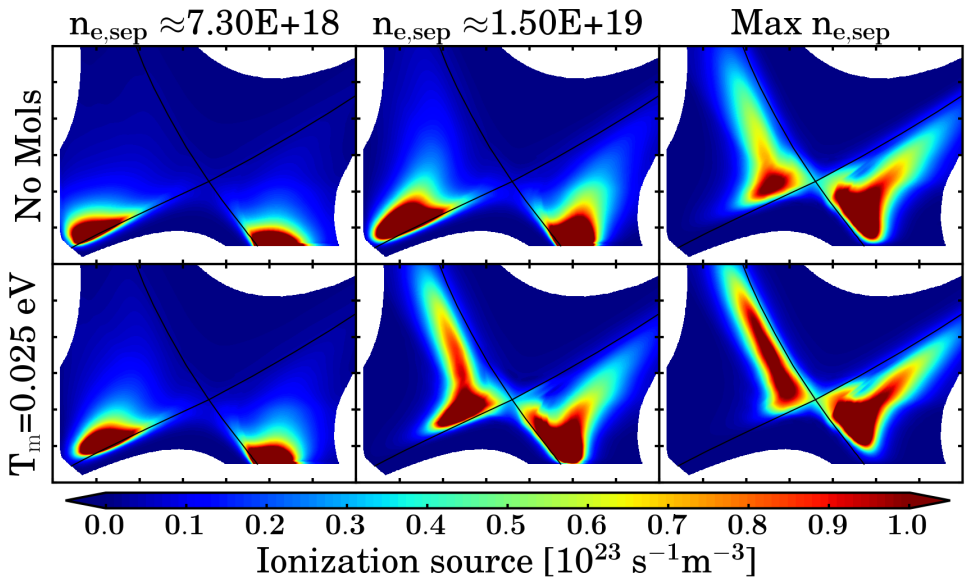

Figure 5.7: Poloidal profiles of the ionization source density for the no-molecule (top row) and molecule (bottom row) simulations. The abscissa in each plot is the major radius, and the ordinate is the vertical distance with the black lines being the magnetic separatrix. Each column represents increasing separatrix density and the last column shows the maximum separatrix density for each model. Here, drifts are excluded.

cases are dominated by hydrogen radiation. The hydrogen losses are driven by resonant line radiation, which are several orders of magnitude higher than the recombination losses. The resulting volumetric power loss region has the same spatial distribution as the ionization region in the UEDGE simulations (Fig. 5.7).

The spatial displacement of the radiation region is accompanied by decreasing total hydrogen losses and increasing total impurity losses in the numerical domain (Fig. 5.2). This is consistent with the fact that impurities radiate more strongly close to the X-point. Note that the densities in the poloidal profiles are chosen so that the leftmost column are conduction-limited cases ($n_{e,sep} \approx 7.3 \times 10^{18}$ m^{-3}), the middle column are cases close to the onset of detachment (roll over in $\mathbf{J}_{ion,peak}$, $n_{e,sep} \approx 1.5 \times 10^{19}$ m^{-3}) and the rightmost column are the maximum $n_{e,sep}$ cases for that setup.

Volumetric recombination, considered to play a central role in plasma detachment (section 2.4.4), is predicted to become significant in detached plasma conditions (Fig. 5.8). From figure 5.8 the detachment of the inner divertor target before the outer divertor target becomes apparent as the

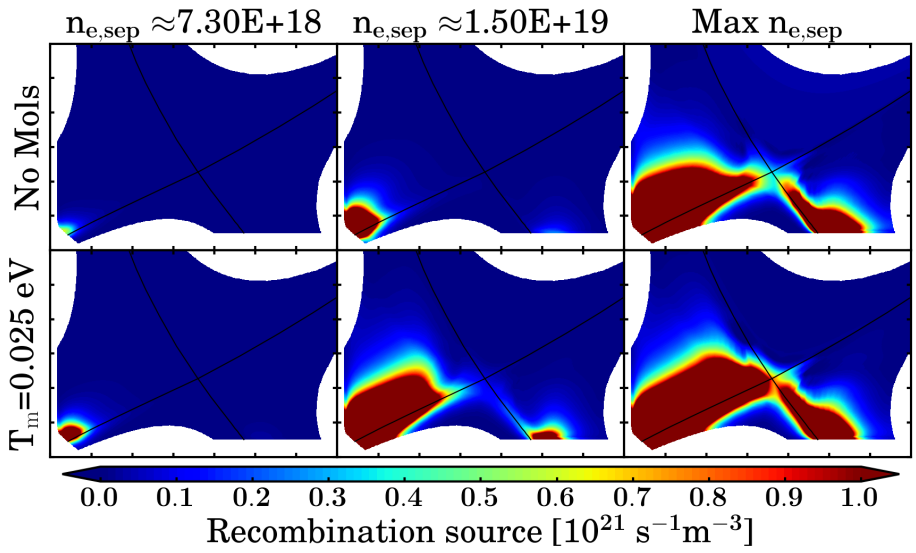

Figure 5.8: Poloidal profiles of the recombination source density for the no-molecule (top row) and molecule (bottom row) simulations. The abscissa in each plot is the major radius, and the ordinate is the vertical distance with the black lines being the magnetic separatrix. Each column represents increasing separatrix density, and the last column shows the maximum separatrix density for each model. Here, drifts are excluded.

volumetric recombination is significantly more pronounced here than at the outer target. The spatial distribution of the volumetric recombination source is the same as that of the electron density, as the recombination rate increases with electron density (Fig. 5.9).

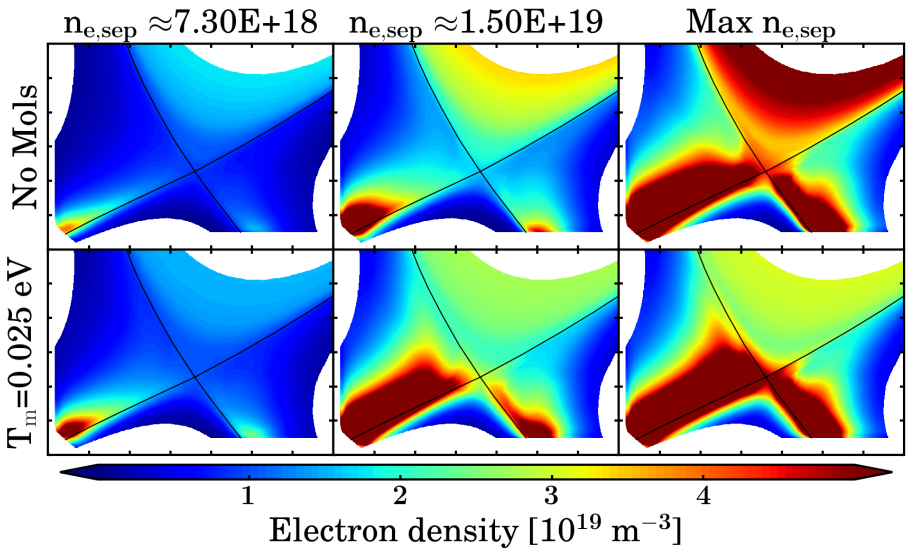

Figure 5.9: Poloidal profiles of the electron density for the no-molecule (top row) and molecule (bottom row) simulations. The abscissa in each plot is the major radius, and the ordinate is the vertical distance with the black lines being the magnetic separatrix. Each column represents increasing separatrix density, and the last column shows the maximum separatrix density for each model. Here, drifts are excluded.

5.2 The impact of drifts

Each set of simulations were carried out with drifts switched on (drift simulations) and off (no-drift simulations). Here, only the no-molecule and molecule simulations where $T_m = 0.025$ eV are presented, as this case is representative of the molecule simulations.

Including drifts in the simulations affects the target plasma pressure, temperatures and ion current densities similarly (Fig. 5.10). The plasma pressure close the separatrix is reduced due to radial $\mathbf{E}\times\mathbf{B}$ drifts transporting the plasma across the separatrix into the PFR where poloidal $\mathbf{E}\times\mathbf{B}$ drifts transport causes a current into the inner divertor leg (Fig. 4.4 and 5.13). As the separatrix density decreases, the ion and electron temperatures of the drift simulations increase at higher rates than the no-drift simulation temperatures. The same behaviour has been observed in previous studies for no-molecule simulations [44]. UEDGE predicts 20% and 60% higher ion temperatures for the drift simulations compared to the no-drift simulations

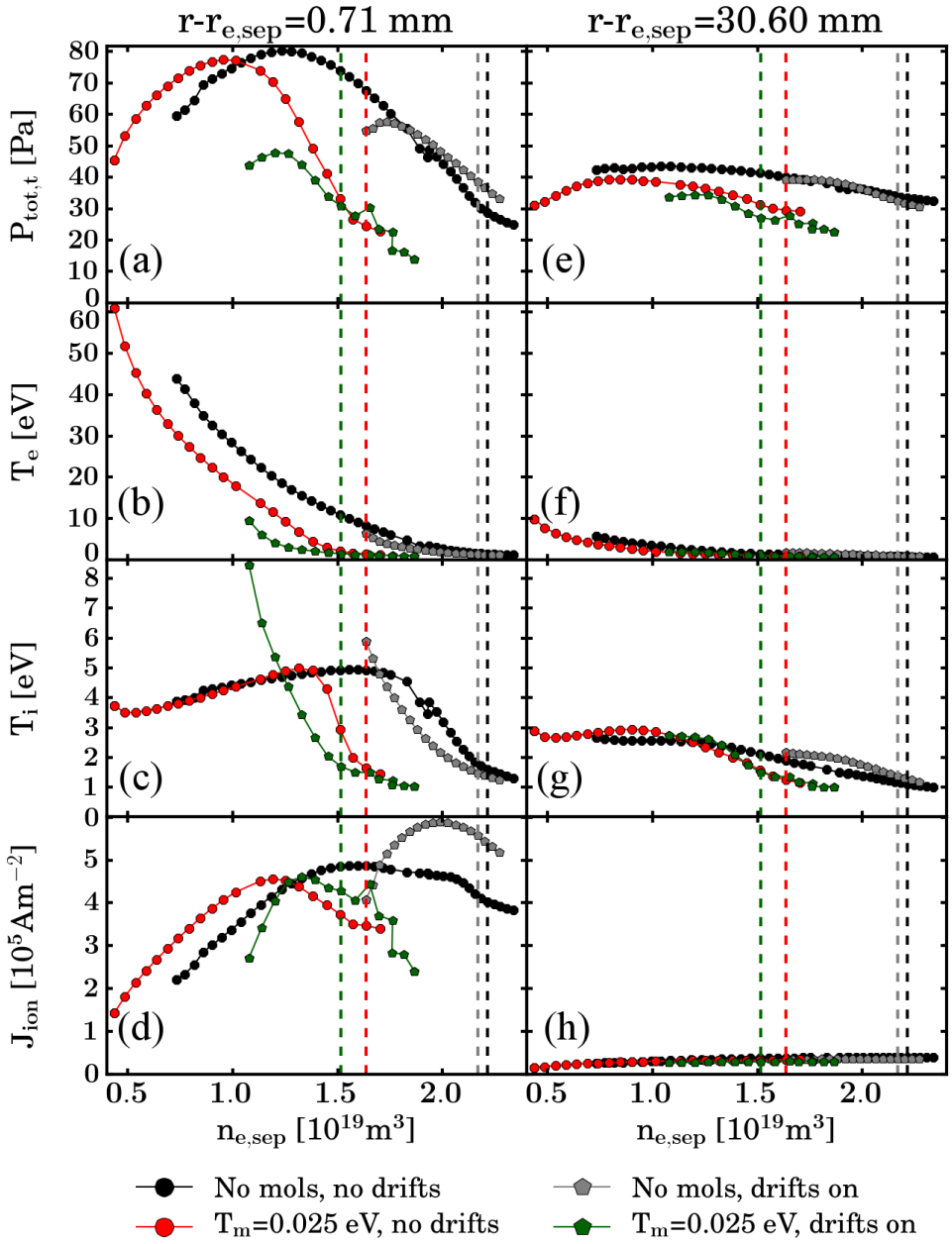

Figure 5.10: Plasma pressure (a,e), electron (b,f) and ion temperatures (c,g) and current density (d,h) in the near SOL (left column) and far SOL (right column) as a function of electron separatrix density. The dashed lines mark the separatrix densities for which $T_{e,peak,OT} < 1.5$ eV, considered as detached conditions, for the simulations with corresponding color. Here, the distances to the separatrix are mapped to the OMP.

for the no-molecule and molecule simulations, respectively. This behavior imposes a low-separatrix density limit of the drift simulation convergence.

UEDGE predicts a local minima in the outer target current densities at $n_{e,sep} \approx 1.8 \times 10^{19}$ m^{-3} and $n_{e,sep} \approx 1.3 \times 10^{19}$ m^{-3} for the no-molecule and molecule simulations, respectively. The no-molecule simulation current density rolls over at 10% higher densities, but there is no increase in the roll over separatrix density for the molecule simulations (Fig. 5.11). The increased roll over density of the no-molecule simulations is consistent with previous results [44]. Here, the current densities incident on the outer target plate of the molecule simulations are decreased more strongly compared to the other setups, indicating stronger detachment at lower separatrix densities (Fig. 5.11). This effect is not present for the no-molecule simulations at these separatrix densities.

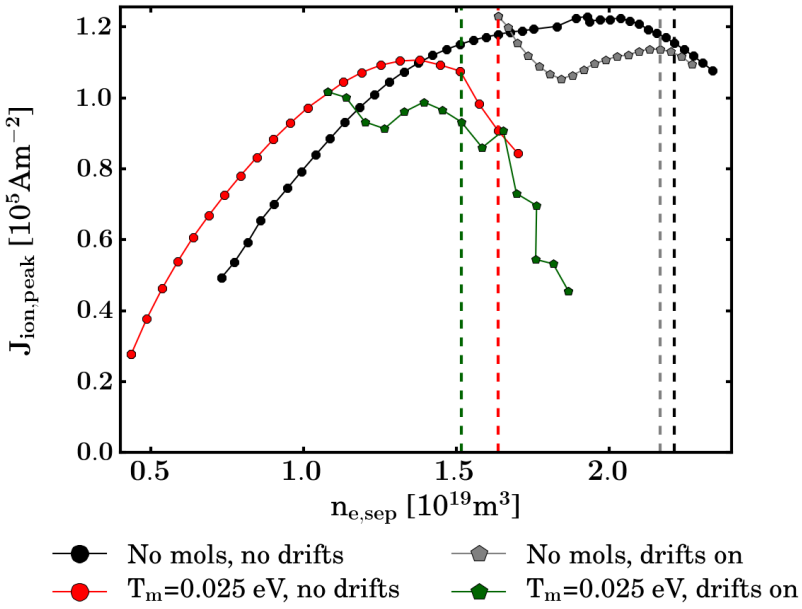

Figure 5.11: Peak current density to the inner divertor plate as a function of electron separatrix density. The peak current density is representative of the peak current incident on the target. The dashed lines mark the separatrix densities for which $T_{e,peak,OT} < 1.5$ eV, considered as detached conditions, for the simulations with corresponding color.

The local minima of the ion current to the outer plate occurs at the same separatrix density ($n_{e,sep} \approx 1.8 \times 10^{19}$ m^{-3}) as the peak target atom density of the drift simulations decreases below the corresponding densities of the no-drift simulations, for the no-molecule simulations (Fig. 5.12b and 5.11).

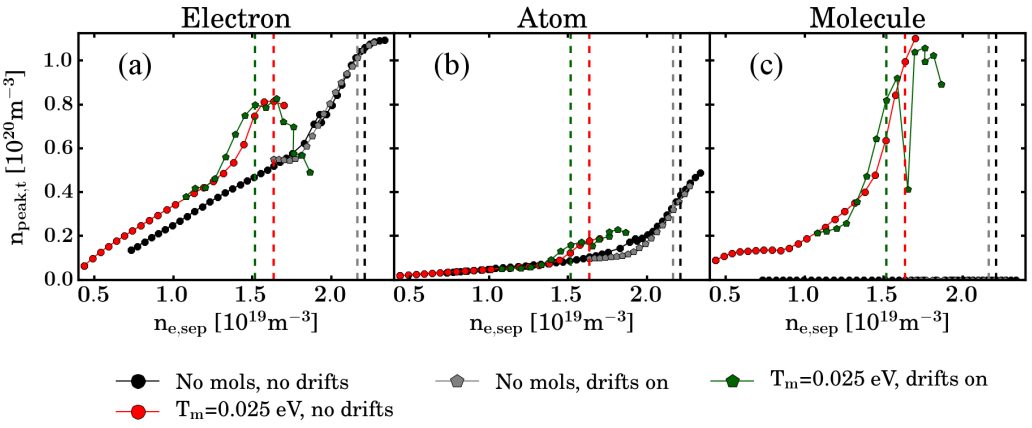

Figure 5.12: Peak target electron (a), deuterium atom (b) and molecule (c) densities as a function of separatrix density for the drift simulations. The dashed lines mark the separatrix densities for which $T_{e,peak,OT} < 1.5$ eV, considered as detached conditions, for the simulations with corresponding color.

For the molecule simulations, the minima corresponds to the peak target molecule densities of the drift simulations decreasing below the corresponding no-drift densities at $n_{e,sep} \approx 1.3 \times 10^{19}$ m^{-3} (Fig. 5.12c and 5.11). The peak target atom density of the no-molecule drift simulations increase to the level of no-drift atom densities at high separatrix densities (Fig. 5.12). The peak target molecule densities of the drift simulation, however, increase to higher densities than the no-drift simulations. This explains why the roll over in current density to the outer plate occurs at the same separatrix density for both the drift and no-drift simulations.

At lower separatrix densities, the molecular simulation peak target densities are higher than the no-drift simulations, the opposite being true for the no-molecule simulations (Fig. 5.12). As the separatrix density increases, the peak target densities of the molecule simulations decrease more rapidly than the no-drift simulations, whereas the no-molecule simulation peak target densities converge towards the no-drift simulation peak target densities (Fig. 5.12).

Including drifts causes a divertor asymmetry with ion and electron density build up at the inner plate (Fig. 5.13). The electron densities of the molecule simulations exceed $n_e \approx 5 \times 10^{19}$ m^{-3} in most of the inner divertor leg for the no-drift simulations, and the additional charged particle influx by the drifts increases the densities further. For the molecule simulations this causes the electron densities in the inner leg to increase up to, and above, the X-

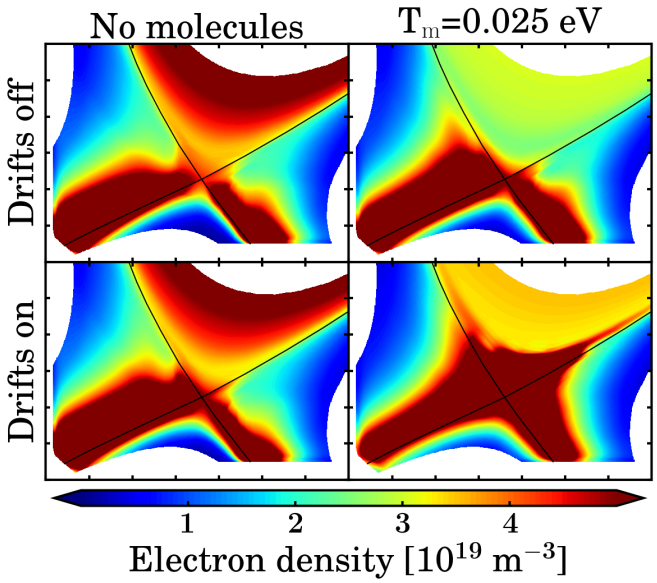

Figure 5.13: Poloidal profiles of divertor electron densities for the no-molecule (left column) and molecule (right column) simulations for the no-drift (upper row) and drift (lower row) simulations at the highest n_{sep} for each setup. The abscissa in each plot is the major radius, and the ordinate is the vertical distance with the black lines being the magnetic separatrix.

point, resulting in the same density in both divertor legs through the X-point (Fig. 5.13). Here, the electron densities are representative of the combined hydrogen and impurity ion densities due to the quasineutrality condition.

The asymmetry in the densities of the no-molecule simulations displaces the volumetric loss region further upstream in the inner leg (Fig. 5.14). At the outer leg, the volumetric loss region is displaced towards the PFR and it is stretched towards the inner leg in the PFR, consistent with figure 4.4 (Fig. 5.14). The displacement of the volumetric loss region results in increased impurity radiation for both the no-molecule and the molecule simulations. The increase in impurity radiation is significantly stronger for the molecule simulations compared to the no-molecule simulations: 64% compared to 13% (Fig. 5.15).

The large increase in impurity radiation for the molecule simulations compared to the no-molecule cases are due to an X-point MARFE [46] forming (Fig. 5.16). The MARFE occurs between separatrix densities between $n_{e,sep} \approx 1.58 \times 10^{19}$ m^{-3} and $n_{e,sep} \approx 1.65 \times 10^{19}$ m^{-3} for the molecule simulations, but is not observed for separatrix densities in excess of $n_{e,sep} \approx 2.3 \times 10^{19}$ m^{-3} for the no-molecule simulations. The MARFE is stable for

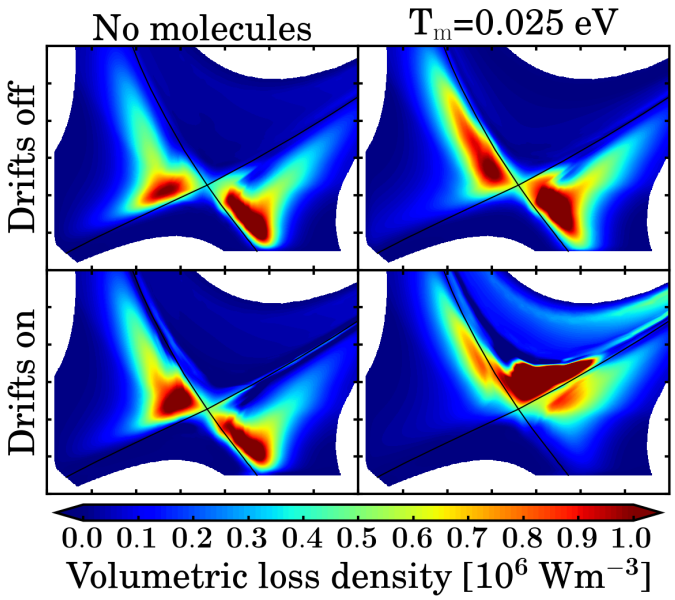

Figure 5.14: Poloidal profiles of divertor power loss densities for the no-molecule (left column) molecule (right column) simulations for the no-drit (upper row) drift (lower row) simulations at the highest n_{sep} for each setup. The abscissa in each plot is the major radius, and the ordinate is the vertical distance with the black lines being the magnetic separatrix.

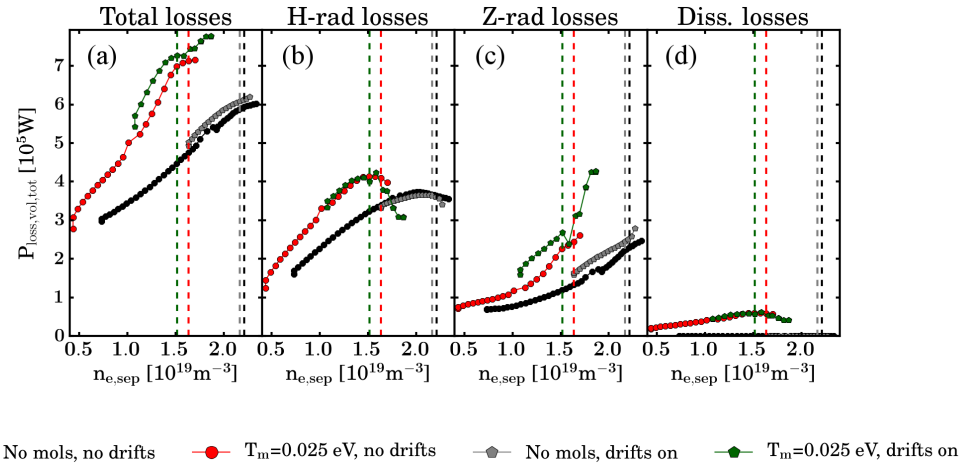

Figure 5.15: Total volumetric power losses (a) and hydrogen (b), impurity (c), and dissociation (d) contributions in the numerical domain as a function of electron separatrix density. The dashed lines mark the separatrix densities for which $T_{e,peak,OT} < 1.5$ eV, considered as detached conditions, for the simulations with corresponding color.

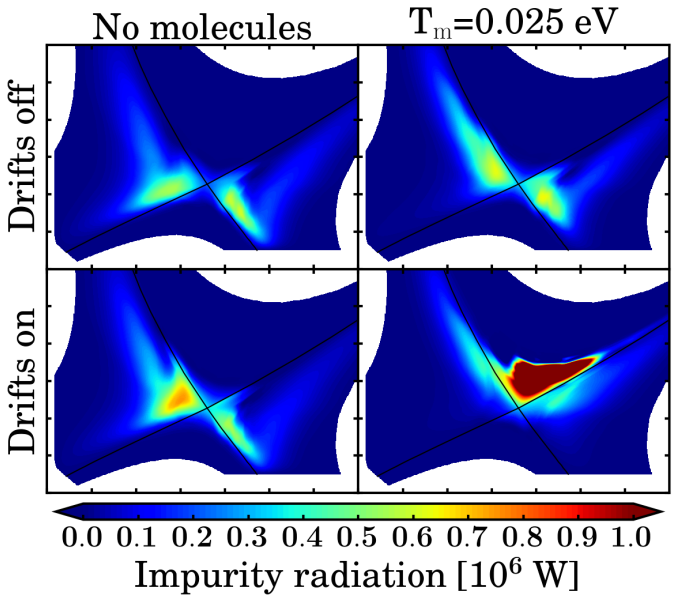

Figure 5.16: Poloidal profiles of divertor impurity radiation for the no-molecule (left column) molecule (right column) simulations for the no-drit (upper row) drift (lower row) simulations at the highest n_{sep} for each setup. The abscissa in each plot is the major radius, and the ordinate is the vertical distance with the black lines being the magnetic separatrix.

densities above this threshold, and increases in strength with increasing separatrix density. The impurity radiation present in the no-molecule simulations is also localized close to the X-point, in accordance with previous studies [47], and is stronger for the drift simulations compared to the no-drift simulations.

The strongly radiating impurities inside the separatrix for the molecule simulations result in temperatures sufficiently low for volumetric recombination within the separatrix (Fig. 5.17). The recombination source is strong as electron densities are high in the divertor legs and at the X-point, and the recombination rate increases with density (Fig. 5.13). Figure 5.8 indicates that including drifts decreases the degree of plasma detachment at the outer target for no-molecule simulations. This is in agreement with previous studies [44]. However, for the molecule simulations the detachment becomes significantly stronger as drifts are considered.

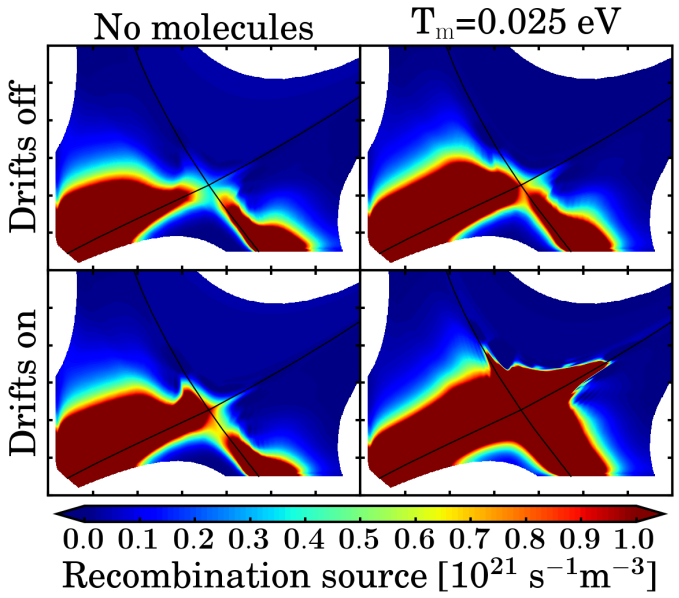

Figure 5.17: Poloidal profiles of divertor recombination source for the no-molecule (left column) molecule (right column) simulations for the no-drit (upper row) drift (lower row) simulations at the highest n_{sep} for each setup. The abscissa in each plot is the major radius, and the ordinate is the vertical distance with the black lines being the magnetic separatrix.

Chapter 6

Discussion

6.1 UEDGE-predicted detachment in atom-only plasmas

The primary power loss processes for the no-molecule simulations are line radiation of hydrogen and the intrinsic impurity carbon. Additionally, ionization decreases the electron temperature by the binding energy, which is carried by the ions. For the no-drift simulations, hydrogen-like radiation (Ly-α) is the dominant loss process. However, at sufficiently high separatrix densities the impurity radiation becomes comparable to the hydrogen radiation.

The onset of detachment is driven by increased atom and neutral molecule densities in front of the targets, enabled by volumetric recombination in the divertor. Volumetric recombination requires temperatures below $T_e \approx 1$ eV (Fig. 4.2) and high electron densities ($\nu_r = n_e\langle\sigma_r v_e\rangle$, eq. 3.21). When the impurity radiation becomes significant, for the no-molecule simulations, the combined contribution of radiation and the sheath and SOL potentials are sufficient to decrease the electron temperature, and increase the electron density, in front of the targets to temperatures below $\sim 1.5\ mathrmeV$. Thus, volumetric recombination occurs in the high electron density regions, detaching the plasma from the targets. This is accompanied by an increase in the atomic density in front of the target (Fig. 6.1).

To achieve divertor detachment at lower separatrix densities more power must be dissipated volumetrically in the SOL. An efficient process for SOL power dissipation is impurity radiation. However, in the no-molecule simulations the impurity radiation contribution to the volumetric power losses remains rather insignificant compared to the molecule simulations, even at separatrix densities above 2×10^{19} m^{-3} (Fig. 5.2). Thus, intrinsic impurity

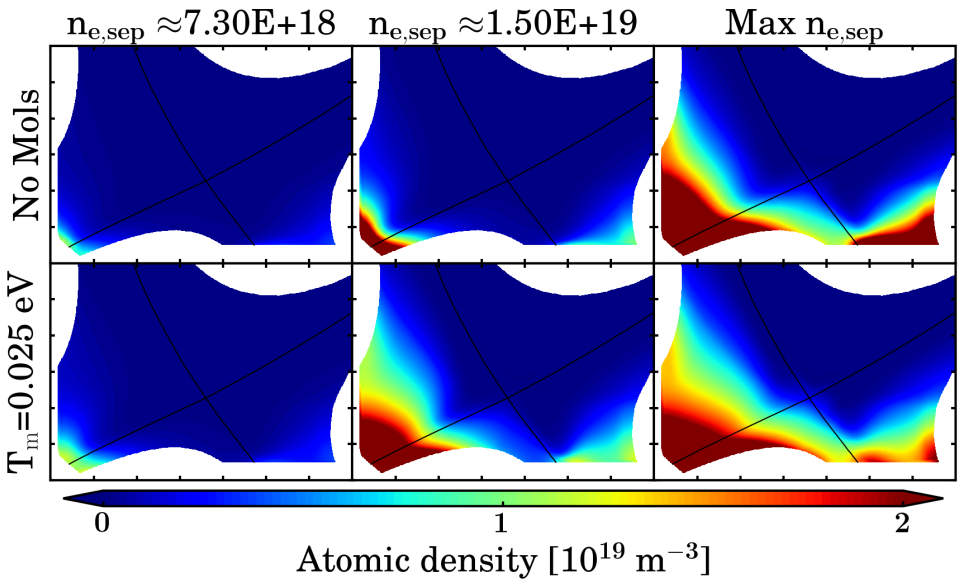

Figure 6.1: Poloidal profiles of the atom density for the no-molecule (top row) and molecule (bottom row) simulations. Each column represents increasing separatrix density and the last column shows the maximum separatrix density for each model. Here, drifts are excluded.

radiation by carbon is only significant for detachment to occur at high separatrix densities. This illustrates the benefits of seeding impurities which can increase the volumetric power losses sufficiently for detachment to occur at lower separatrix densities.

6.2 The impact of molecules of defined temperature on detachment

The molecular model in UEDGE considers the decreased number of recycled particles from the walls and targets, since two hydrogen atoms constitute a molecule. The dissociation energy, here taken to be 10 eV, is lost by the electron population due to the dissociation process. The Franck-Condon energy, here taken to be 2.5 eV per atom from dissociation, is gained by the ion-atom fluid, and the remaining 5 eV is lost as dissociation radiation. Thus, dissociation processes are a volumetric atom and ion-atom energy source and an electron energy sink. Here, the Franck-Condon energy and radiation due to dissociation processes are initial approximations and have not been verified against experimental measurements or theoretical models.

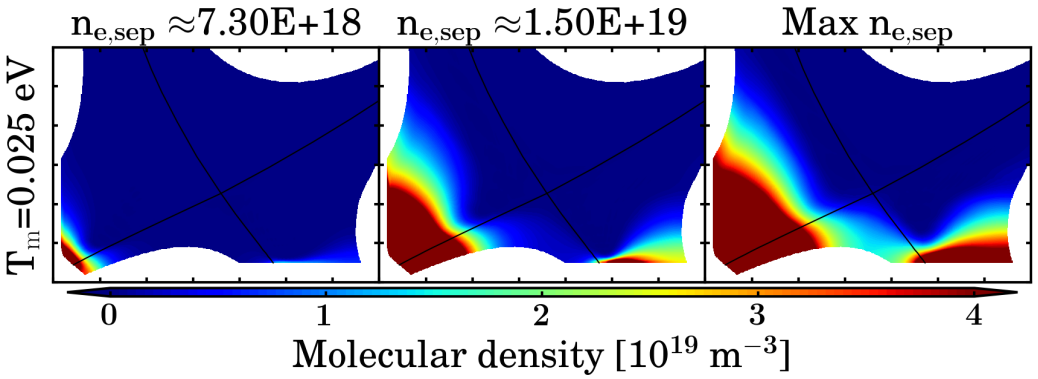

Figure 6.2: Poloidal profiles of the molecular density for the molecule simulations. Each column represents increasing separatrix density and the last column shows the maximum separatrix density. Here, drifts are excluded.

Regions where the dissociation rates become significant ($\sim$ 3 eV, Fig. 4.2), strongly cool the electrons and heats the ion-atom fluid. Additionally, the atomic density in front of the targets decreases as incident hydrogen ions and atoms are recycled as molecules. Thus, detachment is driven by the neutral atoms together with the molecules (Fig. 6.1). In the molecule simulations the molecular density in front of the targets dominates over the atom density (Fig. 6.2 and 6.1).

At low separatrix densities ($n_{e,sep} \approx 1.3\times10^{19}$ m^{-3}) the impact of molecules is small due to the high plasma temperatures (and thus high dissociation rates) in the SOL dissociating the molecules in front of the targets (Fig. 5.1). However, since the plasma is recycled as molecules at the targets, the dissociation energy is lost in the dissociation process close to the targets (Fig. 6.3), which is observed as an $\sim$ 10 eV drop in the electron temperatures at the target (Fig. 5.1). The dissociative electron cooling results in electron temperatures below $\sim$ 1.5 eV at lower separatrix densities (Fig. 5.1b,f). The decrease in electron temperature strongly increases the ion-electron thermal exchange frequency [22] and the ion-electron thermal equipartition, reducing the ion temperatures, as well as increasing the recombination rates (Fig. 4.2), and detaches the plasma. Once the plasma detaches, the molecules will diffuse from the targets according to equation 3.35 to regions where the dissociation rates become significant ($\sim$ 3 eV, Fig. 4.2), expanding the dissociation region further upstream the targets (Fig. 6.3).

The earlier onset of detachment of the molecule simulations compared to the no-molecule simulations is due to strong dissociative electron cooling. The dissociation (10 eV) and Franck-Condon (2.5 eV per atom) energies do,

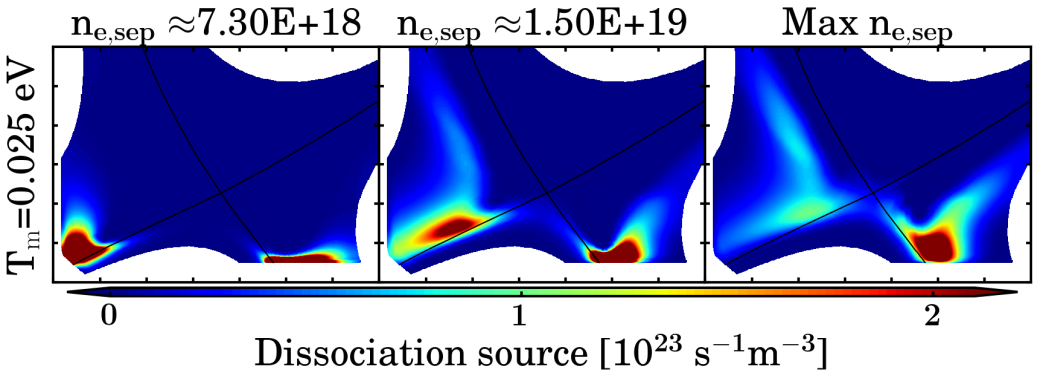

Figure 6.3: Poloidal profiles of the dissociation source for the molecule simulations. Each column represents increasing separatrix density and the last column shows the maximum separatrix density for each model. Here, drifts are excluded.

however, need to be verified. Decreasing the dissociation energy is expected to affect the onset of detachment in UEDGE. Further work with varying dissociation and Franck-Condon energies will be carried out to assess their effect on the UEDGE predictions. If the effect of varying the energies is significant it is important to verify the values used against theory or experimental results.

When considering molecules in UEDGE molecular processes such as MAR, vibrationally excited molecules, and molecular radiation are not considered. Previous studies have shown that recombination plays a significant role in divertor detachment [24] and that the rates of MAR, facilitated by molecular ions, can be significantly higher than three-body recombination [27]. Thus, including molecular ions into the simulations as a charged fluid species could provide a valuable insight into molecular processes. Also considering vibrationally excited molecules could impact the simulations as these molecules have higher dissociation rates than vibrationally relaxed molecules. The vibrational modes could be considered by finding the distribution of vibrationally excited molecules in fusion relevant plasmas. The dissociation rates, which are a superposition of the dissociation rates of the individual modes, could be constructed and considered in UEDGE.

6.3 Impact of increasing molecular temperature on divertor conditions

Increasing the molecular temperature shifts the pressure, temperature, current density and volumetric power loss curves to higher separatrix densities (Figs. 5.1,5.4, and 5.2). The UEDGE model used for user-defined molecular temperature does not consider thermal equipartition between molecules and ions or atoms. Thus, increasing the molecular temperature only influences the molecule velocity indirectly through the pressure gradient (∇p_m) by enabling steeper molecular gradients (eq. 3.35) and by providing more energy to the atoms resulting from dissociation. The shift of plasma temperature, pressure, and current density to higher separatrix densities is equivalent, but unrelated, to an increase in plasma core power. Thus, the conclusion is that increasing the molecular temperature of the molecules increases the total power in the numerical domain for the UEDGE user-defined molecular temperature model.

6.4 The impact of drifts

For configurations with the ion ∇B drift in the direction of the lower divertor cause a divertor asymmetry across the inboard side [44]. The drifts transport plasma towards the inner target, decreasing the outer target densities, thus, shifting the detachment onset at the outer plate to higher separatrix densities for the no-molecule simulations. For the molecule simulations, with $T_m = 0.025$ eV, the inclusion of drifts result in a stable X-point MARFE at densities above $1.58 - 1.65 \times 10^{19}$ m^{-3}. This threshold increases by $\sim$15% as the molecular temperature is increased to $T_m = 0.5$ eV.

The drift-driven flows cause an increase in plasma density in the inner divertor leg further upstream towards the X-point when drifts are considered, which can be observed for both the no-molecule and molecule simulations. The density in the inner leg is significantly higher for the molecule simulations compared to the no-molecule simulations when drifts are excluded. Thus, when the drifts are switched on the increase in densities further upstream is sufficient for a high-density front to form across the X-point region for the molecule simulations. This high-density front connects the divertor legs and the core domain and is postulated to cause the X-point MARFE. The energy in the core region is efficiently radiated away by the partially ionized impurities, decreasing the local temperature. The temperature decrease is sufficient for volumetric recombination within the separatrix along the high-

density front.

The X-point MARFE explains why there is no increase in separatrix density for the current density roll over. The X-point MARFE results in stronger detachment of the molecule simulations considering drifts at the same separatrix densities compared to the no-drift simulations. The X-point MARFE could occur due to distinct regimes of the SOL plasma when molecules are considered, or appear for the no-molecule simulations at sufficiently high separatrix densities. The separatrix density for the no-molecule simulations should be increased further in order to determine which is the case. If the same effect is observed for the no-molecule simulations at sufficiently high separatrix densities, then the outcome cannot be attributed to molecular effects.

However, the processes causing the high-density front in both divertor legs and core domain to occur is not yet fully understood. Investigations need to be conducted to determine under which conditions the high-density front occurs, and which processes are driving ion density buildup above the X-point.

6.5 The UEDGE reaction and scattering rates

The UEDGE ionization, recombination, and dissociation rates were found to be within 20%, 8%, and 44% of their ADAS and AMJUEL equivalents, respectively. For CX the UEDGE and AMJUEL rates were a factor of ~ 3 higher than the ADAS rates at temperatures below 1 eV. The UEDGE elastic scattering rates were found to be approximately one order of magnitude smaller than the AMJUEL elastic scattering rates. Since UEDGE uses the elastic scattering rates for calculating a number of processes, such as the kinetic thermal conductivity, thermal equipartition and diffusive velocities of the atoms and molecules, a thorough investigation into the elastic scattering rates must be conducted to determine them with confidence.

However, the AMJUEL rates for CX and elastic scattering were determined by the plasma temperature and particle impact energy, rather than by plasma temperature and density like to other rates. Thus, further investigations regarding how to relate the plasma conditions to the the energy of the colliding particles must be undertaken to confidently compare the UEDGE and AMJUEL CX and elastic scattering rates.

Chapter 7

Conclusions

The work conducted in this thesis investigated the impact of molecules on plasma detachment as predicted by the edge fluid code UEDGE for low-confinement mode (L-mode) divertor plasma conditions in the DIII-D tokamak. UEDGE simulations were carried out with deuterium molecules being excluded and included. The molecular model used considers molecules of user-defined temperature in the UEDGE numerical domain. Here, the simulations considering molecules were carried out for spatially constant molecular temperatures of $T_m = 0.025$ eV, $T_m = 0.1$ eV, $T_m = 0.5$ eV, and $T_m = 1$ eV. The simulations were run for a magnetic configuration with ion ∇B drifts in the direction of the lower divertor with cross-field drifts excluded and included.

The no-drift simulations indicate that when molecules are considered the plasma detaches at 25% lower separatrix densities compared to when molecules are not included. This effect was attributed to strong Franck-Condon cooling of the electrons associated with molecular dissociation, here set to 10 eV. Increasing the molecular temperature from 0.025 eV to 1 eV was found to shift the plasma detachment to 9% higher separatrix densities. This was attributed to the hotter molecules increasing the total energy in the numerical domain.

UEDGE simulations with cross-field drifts included predict higher plasma densities at the inner target plate and divertor leg. This increases the separatrix densities required for plasma detachment in the no-molecule simulations. For the molecule simulations assuming $T_m = 0.025$ eV, the inclusion of drifts results in a stable X-point MARFE at densities above $n_{e,sep} \approx 1.58 - 1.65 \times 10^{19}$ m^{-3}. This threshold increases by $\sim$15% as the molecular temperature is increased to $T_m = 0.5$ eV. A high-density region between the inner and outer divertor legs forms in the core domain across the X-point region for the cases considering molecules. The high-density front inside

the core domain is postulated to cause the MARFE due to the buildup of strongly radiating intrinsic impurities. The impurity line radiation losses cools the plasma sufficiently for recombination to occur in the dense volume inside the separatrix. This effect appears to be due to a further increase in plasma density in the inner leg, which already high for the molecular simulations when drifts are excluded, due to drift-driven flows.

The UEDGE-predicted ionization, recombination and dissociation rates were found to be within 20%, 8%, and 44%, respectively, of the corresponding ADAS and AMJUEL rates. However, the charge-exchange process rates in UEDGE differed by up to a factor of 3 compared to the ADAS rates at low ion temperatures. The UEDGE elastic scattering rates were found to be an order of magnitude smaller than the AMJUEL rates, which enhances the transport in UEDGE.

Bibliography

[1] International Energy Agency, *World energy outlook 2017*, OEC/IEA, 2017.

[2] E. A. Ainsworth et al., *What have we learned from 15 years of free-air CO2 enrichment (FACE)? A meta-analytic review of the responses of photosynthesis, canopy properties and plant production to rising CO2*, New Phytologist **165** (2005) 351.

[3] T. J. Dolan, R. W. Moir, W. Manheimer, L. C. Cadwallader, and M. J. Neumann, *Magnetic fusion technology*, Springer, 2017.

[4] Max-Planck-Institut für Plasmaphysik, *SOLPS 5.0*, `http://solps-mdsplus.aug.ipp.mpg.de:8080/solps/Documentation/solps.pdf`, 2013, [Online; accessed 06-April-2018].

[5] R. Simonini et al., *Models and numerics in the multi-fluid 2-D edge plasma code EDGE2D/U*, Contributions to Plasma Physics **34** (1994) 368.

[6] S. Wiesen, *EDGE2D/EIRENE code interface report*, `http://www.eirene.de/e2deir_report_30jun06.pdf`, 2006, [Online; accessed 06-April-2018].

[7] T. D. Rognlien and M. E. Rensink, *Users manual for the uedge edge-plasma transport code*, Lawrence Livermore National Laboratory, 2017.

[8] D. Reiter, *The EIRENE code user manual including: B2-EIRENE interface*, `http://www.eirene.de/eirene.pdf`, 2017, [Online; accessed 06-April-2018].

[9] G. D. Porter et al., *Simulation of experimentally achieved DIII-D detached plasmas using the UEDGE code*, Physics of Plasmas **3** (1996) 1967.

[10] G. D. Porter et al., *Detailed comparison of simulated and measured plasma profiles in the scrape-off layer and edge plasma of DIII-D*, Physics of Plasmas **7** (2000) 3663.

[11] T. D. Rognlien et al., *Comparison of 2D simulations of detached divertor plasmas with divertor Thomson measurements in the DIII-D tokamak*, Nuclear Materials and Energy **12** (2017) 44.

[12] K. S. Krane and D. Halliday, *Introductory nuclear physics*, John Wiley & Sons, 1988.

[13] J. Wesson and D. J. Campbell, *Tokamaks*, third ed., Oxford University Press, 2004.

[14] J. P. Freidberg, *Plasma physics and fusion energy*, Cambridge university press, 2007.

[15] M. Keilhacker et al., *High fusion performance from deuterium-tritium plasmas in JET*, Nuclear Fusion **39** (1999) 209.

[16] J. D. Lawson, *Some criteria for a power producing thermonuclear reactor*, Proceedings of the Physical Society. Section B **70** (1957) 6.

[17] EUROfusion, *EDGE2D/EIRENE code interface report*, `http://www.euro-fusion.org`, 2018, [Online; accessed 17-April-2018].

[18] P. C. Stangeby, *The plasma boundary of magnetic fusion devices*, Institute of Physics Publishing Bristol and Philadelphia, 2000.

[19] K. Kamiya et al., *Edge localized modes: recent experimental findings and related issues*, Plasma Physics and Controlled Fusion **49** (2007) S43.

[20] D. Bohm, *The characteristics of electrical discharges in magnetic fields*, McGraw-Hill, 1949.

[21] W. Fundamenski, *Parallel heat flux limits in the tokamak scrape-off layer*, Plasma physics and controlled fusion **47** (2005) R168.

[22] L. Spitzer, *Physics of fully ionized gases*, Interscience Publishers, New York, 1956.

[23] A. Kallenbach et al., *Partial detachment of high power discharges in ASDEX Upgrade*, Nuclear Fusion **55** (2015) 053026.

[24] S. I. Krasheninnikov et al., *Plasma recombination and divertor detachment*, Physics Letters A **214** (1996) 285.

[25] Figure courtesy of Dr. Sven Wiesen, Forschungszentrum Juelich, Germany, March 2018.

[26] D. Lumma et al., *Radiative and three-body recombination in the Alcator C-Mod divertor*, Physics of Plasmas **4** (1997) 2555.

[27] S. I. Krasheninnikov, *Molecule assisted recombination (MAR): Mechanisms and plasma conditions for effective operation*, Physica Scripta **T96** (2002) 7.

[28] U. Fantz et al., *Franck–Condon factors, transition probabilities, and radiative lifetimes for hydrogen molecules and their isotopomeres*, Atomic Data and Nuclear Data Tables **92** (2006) 853.

[29] R. Fitzpatrick, *Introduction to plasma physics*, The University of Texas at Austin: s.n., 2008.

[30] S. Chapman and T. G. Cowling, *The mathematical theory of non-uniform gases: an account of the kinetic theory of viscosity, thermal conduction and diffusion in gases*, Cambridge university press, 1970.

[31] S. I. Braginskii, *Transport Processes in a Plasma*, Reviews of Plasma Physics **1** (1965) 205.

[32] T. D. Rognlien et al., *A fully implicit, time dependent 2-D fluid code for modeling tokamak edge plasmas*, Journal of Nuclear Materials **196** (1992) 347.

[33] L. L. Lao et al., *Reconstruction of current profile parameters and plasma shapes in tokamaks*, Nuclear fusion **25** (1985) 1611.

[34] B. J. Braams, *Computational studies in tokamak equilibrium and transport*, PhD, Rijksuniversitet Utrecht, 1986.

[35] T. D. Rognlien et al., *Pseudoclassical transport equations for magnetized edge-plasmas in the slab approximation*, Plasma Physics Reports **25** (1999) 943.

[36] P. N. Brown et al., *Matrix-free methods for stiff systems of ODE's*, SIAM Journal on Numerical Analysis **23** (1986) 610.

[37] Y. Saad, *Iterative methods for sparse linear systems*, vol. 82, Society for Industrial and Applied Mathematics, Philadelphia, 2003.

[38] T. D. Rognlien et al., *Two-dimensional electric fields and drifts near the magnetic separatrix in divertor tokamaks*, Physics of Plasmas **6** (1999) 1851.

[39] H. P. Summers, *The ADAS User Manual, version 2.6*, `http://www.adas.ac.uk/`, 2018.

[40] D. Reiter, *The data file AMJUEL: Additional Atomic and Molecular Data for EIRENE*, `http://www.eirene.de/amjuel.pdf`, 2017, [Online; accessed 06-April-2018].

[41] M. Keilhacker et al., *Scrape-off layer model for the study of impurity retention in the pumped divertor planned for JET*, Nuclear Fusion **31** (1991) 535.

[42] Y. L. Igitkhanov, *Impurity transport at arbitrary densities in the divertor plasma*, Contributions to Plasma Physics **28** (1988) 477.

[43] M. Groth et al., *Role of cross-field drifts in the onset of divertor detachment*, APS Meeting Abstracts, 2015.

[44] E. Jaervinen, A et al., *Investigations of the impact of cross-field drifts on divertor detachment in DIII-D with UEDGE*, Tech. report, Lawrence Livermore National Laboratory (LLNL), Livermore, CA, 2016.

[45] T. D. Rognlien et al., *Influence of $E\times B$ and ∇B drift terms in 2-D edge/SOL transport simulations*, Journal of nuclear materials **266** (1999) 654.

[46] B. Lipschultz, *Review of MARFE phenomena in tokamaks*, Journal of Nuclear Materials **145** (1987) 15.

[47] S. I. Krasheninnikov et al., *Stability of the detachment front in a tokamak divertor*, Journal of nuclear materials **266** (1999) 251.